Stony Brook University

Numerical modeling in turbulent mixing flows

A Dissertation Presented

by

Hyunkyung Lim

to

The Graduate School in Partial Fulfillment of the Requirements for the

Degree of

Doctor of Philosophy

in

Applied Mathematics and Statistics

Stony Brook University

August 2009

Stony Brook University

The Graduate School

Hyunkyung Lim

We, the dissertation committee for the above candidate for the Doctor of Philosophy degree, hereby recommend acceptance of this dissertation.

James Glimm
Advisor
Department of Applied Mathematics and Statistics

Xiaolin Li
Chairman
Department of Applied Mathematics and Statistics

Xiangmin Jiao
Member
Department of Applied Mathematics and Statistics

Foluso Ladeinde
Outside Member
Department of Mechanical Engineering

This dissertation is accepted by the Graduate School.

Lawrence Martin
Dean of the Graduate School

Abstract of the Dissertation

Numerical modeling in turbulent mixing flows

by

Hyunkyung Lim

Doctor of Philosophy

in

Applied Mathematics and Statistics

Stony Brook University

2009

We are concerned with the chaotic flow fields of turbulent mixing. Chaotic flow is found in an extreme form in multiply shocked Richtmyer-Meshkov unstable flows. The goal of a converged simulation for this problem is twofold: to obtain converged solutions for macro solution features, such as the trajectories of the principal shock waves, mixing zone edges, and mean densities and velocities within each phase, and also for such micro solution features as the joint probability distributions of the temperature and species concentration or a chemical reaction rate. We introduce parameterized subgrid models of mass and thermal diffusion, to define the large eddy simulation (LES) that replicate the micro features observed in the direct numerical simulation (DNS). The Schmidt numbers and Prandtl numbers are chosen to represent typical liquid,

gas and plasma parameter values. Our main result is to explore the variation of the Schmidt, Prandtl and Reynolds numbers by three orders of magnitude, and the mesh by a factor of 8 per linear dimension (up to 3200 cells per dimension), to allow exploration of both DNS and LES regimes and verification of the simulations for both macro and micro observables. We study mesh convergence for key properties describing the molecular level of mixing, including chemical reaction rates between the distinct fluid species.

Methodologically, the results are also new. In common with the shock capturing community, we allow and maintain sharp solution gradients, and we enhance these gradients through use of front tracking. In common with the turbulence modeling community, we include subgrid scale models with no adjustable parameters for LES. These two methodologies have not been previously combined. In contrast to both of these methodologies, our use of Front Tracking, with DNS or LES resolution of the momentum equation at or near the Kolmogorov scale, but without resolving the Batchelor scale, allows a feasible approach to the modeling of high Schmidt number flows.

Key Words: Turbulence, Subgrid models, Large eddy simulation, Direct numerical simulation, Mass diffusion, Thermal diffusion, Schmidt numbers, Prandtl numbers

To my parents

Table of Contents

List of Figures

List of Tables

Acknowledgements

I would like to express my profound gratitude to my advisor, Professor James Glimm, for suggesting this important and exciting thesis topic and for his advice, support, encouragement and guidance toward my Ph. D. degree. He taught me not only the way to do scientific research, but also the way to become a professional scientist. He was always enthusiastic about my education. He is my advisor and a lifetime role model for me.

I am deeply indebted to the support of Professor Xiaolin Li. He provided encouragement and valuable technical knowledge and helped me maintain my focus on the research. I would also like to thank Professor Foluso Ladeinde for being on my dissertation committee.

I would like to thank Professor Xiangmin Jiao and Roman Samulyak, Drs. John Grove and David H. Sharp from whom I have learned many important scientific and mathematical skills.

I would like to thank all my friends during my years of study as a graduate student at Stony Brook for their friendship and encouragement. In particular, I would like to mention Drs. Yan Yu, Wurigen Bo and Daesang Kim, Tulin Kaman, Justin Iwerks, Xingtao Liu, Lingling Wu, Brian Fix. They have shared with me many interesting and inspiring ideas.

Throughout my academic career, the constant support of my parents has always motivated me to strive forward. Their unconditional love has never been affected by the physical distance between us. My dissertation is dedicated to them.

Chapter 1

Introduction

1.1 Overview and Motivation

Turbulence is a prototypical multiscale problem, with a cascade of length scales generally too broad to be modeled effectively by explicit numerical algorithms. The dimensionless Reynolds number governs this process. Turbulent mixing couples turbulence to a concentration equation and introduces the Schmidt number and the Prandtl number as dimensionless parameters. We consider flows which are compressible and which couple the concentration equation actively into the flow dynamics (due to a density contrast, measured by the dimensionless Atwood number $A = (\rho_2 - \rho_1)/(\rho_2 + \rho_1)$, with $A > 0$). These two properties introduce features into the modeling not present in theories of passive scalar transport by a turbulent field [2, 43]. Acceleration driven turbulent mixing is a classical hydrodynamical instability, in which acceleration is directed across a fluid interface separating distinct fluids of different densities [53]. Steady acceleration of a density discontinuity defines the classical Rayleigh-Taylor (RT) instability and impulsive acceleration produced by a

shock wave passing through the fluids defines the Richtmyer-Meshkov mixing. We are concerned with the Richtmyer-Meshkov (RM) instability.

Numerical modeling of turbulence requires removal of degrees of freedom, so that the ones that remain can fit into a feasible computation. There are three numerical models in the computation such as Reynolds averaged Navier-Stokes simulations (RANS), large eddy simulations (LES) and direct numerical simulations (DNS). Removal of fluctuations, to study statistically mean quantities leads to RANS equations. Removal of small length scales, to study the large scale flow features leads to LES, while the restriction to small scale problems allows DNS, in which all transport effects are fully resolved. These terms have analogous meanings in the case of turbulent mixing. Both RANS and LES call for closure models, to introduce the influence of the omitted scales upon those computed. LES are formulated in terms of an averaging procedure. When this average is replaced by the mesh block average over the computational grid, the LES method is called implicit (ILES). The closure models generally contain parameters which are set by comparison to a more exact computation. In this sense LES and DNS (and physical experiments to the extent available) are used to validate the parameters in RANS models and DNS is used to validate those in an LES model.

Since we recognize at the outset that it is not possible to represent all details of a turbulent mixing flow in a feasible computation, we list here the types of observables we would hope to compute correctly. The most important macroscopic variables are those which define the mixing zone, that is the edge position for the mixing zone as a function of time, and the time dependent

locations of the principal shock waves (if any) which play a role in defining it. Additional macroscopic variables which serve to define the flow include the dominant size of the bubbles (light fluid inclusions in the heavy fluid) and mean fluctuations of the mixing zone edge. From the point of view of turbulent combustion, the microscopic (atomic) properties of the mixture are important, to specify the stochiometry needed for combustion. According to [47], the joint probability distribution of the species concentrations and of the temperature is a required input for LES combustion models.

1.2 Front Tracking Method

Discontinuities in the solutions of nonlinear conservation laws are a primary difficulty for numerical simulations. Commonly used numerical schemes are convergent at higher order only for smooth solutions. At discontinuities, the local truncation errors are first order and the solutions are not convergent in a point-wise sense. For nonlinear discontinuities, the width of the solution error region does not grow in time, and is generally about two mesh blocks, but for linear discontinuities, the error region is wider, some five mesh blocks, and is generally growing in time. The front tracking method was introduced [17–19, 26–28] to solve the discontinuity problem, especially for the representation of linear discontinuity such as fluid layer boundaries. The front tracking method is initiated by Richtmyer and Morton [51] and extensive work on the front tracking method has been carried out by J. Glimm and his coworkers [6, 15, 18, 19, 21, 26–28]. The method has been implemented and developed in a robust and validated code called *FronTier* [17–20]. The front tracking

method tracks a discontinuity interface by using analytical solutions of Riemann problems across the interface, and it applies a finite difference scheme to solve the equation on different sides of the discontinuity interface by using the ghost cell extrapolation method [21, 26]. This ghost cell method was also used in tracking using the level set method [12, 13]. The ghost cell method does not preserve conservation at the cells cut by the interface and it has less than first order accuracy at discontinuities. The algorithm is conservative for interior regular cells, but it is not conservative at the irregular cells near the interface. A fully conservative front tracking algorithm has been implemented in *FronTier*. The algorithm is based on the previous works [22–25, 36, 37] with dimensional generalization and algorithmic refinement. Also there are some pioneer works on the conservative tracking algorithms by Chern and Colella [5], Pember, Bell and Colella [44], Swartz and Wendroff [54], and the early one by Harten and Hyman [29]. In this algorithm the front is tracked as a space time surface (three dimensions in the four dimensional space time, for the case of three spatial dimensions). The space time cells cut by this surface are differenced using a finite volume approach. We will give a brief review of the front tracking and fully conservative front tracking algorithm in the *FronTier* code.

1.2.1 Front Tracking Algorithm

The front tracking method in the *FronTier* is performed by two main steps. The first is to propagate and update the front dynamically. The second is to update the interior states.

In the interface propagation, the interface points are first propagated normally. By computing the solution to the local Riemann problem with initial states being those on either side of the interface point and using the method of characteristics, a wave speed and a new position for the interface point are determined. The interface states are then updated by a tangential sweep, which uses a chosen interior solver with a stencil centered at the new interface point.

After interface propagation, we get a new interface at new time level. Any tangles in the new interface are need to be resolved. To resolve this problem and reduce the variance in size and aspect ration of the segments (2D) or triangles (3D) making up the interface, the new interface need to be reconstructed. There are three types of interface reconstruction such as the grid based (GB) interface tracking [39], the grid free (GF) interface tracking [15, 18, 19] and the locally grid based (LGB) interface tracking. Fig. 1.1 shows examples of these three types of interface reconstruction in 2D. A grid free interface is independent of the underlying grid. By reconstruction, all the points on a grid based interface lie on the cell edges. Thus, the interface elements are constructed from vertices which are the intersections between the interface and the grid lines. The grid free interface uses the locally grid based (LGB) method [10] to resolve topological bifurcations. The LGB method uses the GF interface except at a region of space and time where interface entities intersect with each other (or with itself). When such a topological bifurcation occurs, we first isolate the troubled region using a minimized but sufficient box to contain the bifurcation. We then use the GB method to reconstruct

the interface inside the box. Finally, we relink the interface segment inside the box with the ambient grid free interface. The LGB method combines the robustness of the grid based method with the accuracy of grid free method. It is thus a significant improvement to both of these algorithms.

As the next step, we update all the interior states on cell centers. A connected region in the domain separated by the interface is represented by a component. Therefore, each grid node is associated with a specific component in addition to the state variables. The interior states are updated by finite difference schemes.

1.2.2 Conservative Front Tracking Algorithm

Consider a system of hyperbolic conservation laws in N spatial dimension in differential form

$$\frac{\partial U}{\partial t} + \nabla \cdot F(U) = 0, \quad F = (f_1, f_2, ..., f_N) \quad , \tag{1.1}$$

where $U \in R^p$ and $f_j(U) = (f_{1j}(U), ..., f_{pj}(U))^T \in R^p$ are defined in a spatial domain $\Omega \subset R^N$.

Integrating (1.1) in a time-space domain $\mathcal{V} \subset R^{N+1}$, we obtain the integral form of (1.1),

$$\int_{\mathcal{V}} (\frac{\partial U}{\partial t} + \nabla \cdot F(U)) d\mathcal{V} = 0 \ . \tag{1.2}$$

By the divergence theorem, we have

$$\int_{\partial \mathcal{V}} (U, F(U)) \cdot n dS = 0 \ . \tag{1.3}$$

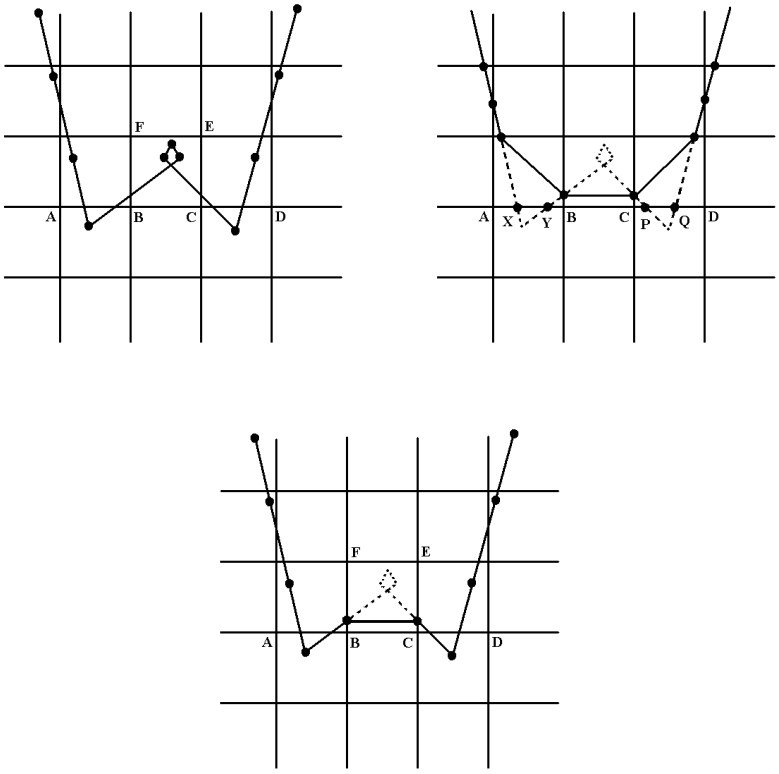

Figure 1.1: A sample of three types of interface representations. Upper-left: grid free (GF) interface; Upper-right: grid based (GB) interface; Lower: locally grid based (LGB) interface.

The finite difference method presented here is an explicit finite volume integration scheme based on the integral form (1.3).

Assume a space-time discretization $\{\mathcal{V}_i\}$ which conforms to the space-time interface as U evolves in one time step from t_n to t_{n+1}. We solve (1.3) explicitly in this region. We define each $\mathcal{V}_i$ as a space-time control volume, and $\partial\mathcal{V}_i = D_i^n \cup D_i^{n+1} \cup \hat{S}_i$ with D_i^n, D_i^{n+1}, and $\hat{S}_i$ meet at most at their boundaries, where D_i^n and D_i^{n+1} are the boundary surfaces of $\mathcal{V}_i$ at time level n and $n+1$ respectively, and $\hat{S}_i$ is the complementary boundary surface of $\mathcal{V}_i$. Dividing the calculation of the integral (1.3) into three parts over D_i^n, D_i^{n+1} and $\hat{S}_i$ respectively, we have

$$|D_i^{n+1}|\overline{U}\,|_{t_{n+1}} = |D_i^n|\overline{U}\,|_{t_n} - \int_{\hat{S}_i} (U, F(U)) \cdot n dS \ , \tag{1.4}$$

where

$$\overline{U}\,|_{t_n} = \frac{1}{|D_i^n|} \int_{|D_i^n|} U(x_1, ..., x_N, t_n) dx_1 ... dx_N$$

and

$$\overline{U}\,|_{t_{n+1}} = \frac{1}{|D_i^{n+1}|} \int_{|D_i^{n+1}|} U(x_1, ..., x_N, t_{n+1}) dx_1 ... dx_N$$

are cell averages, $|D_i^n|$ is the face area of D_i^n, $|D_i^{n+1}|$ is the face area of D_i^{n+1}, and n is the outward normal of $\hat{S}_i$. Therefore, $\overline{U}\,|_{t_{n+1}}$, is the solution to (1.4) at time t_{n+1}.

To calculate $\overline{U}\,|_{t_{n+1}}$, we first need to determine the space-time control volume $\{\mathcal{V}_i\}$. Then we calculate the fluxes defined on the surfaces of $\mathcal{V}_i$, so that we can apply (1.4).

Eq. (1.4) degenerates into a static finite volume scheme

$$\overline{U}\mid_{t_{n+1}} = \overline{U}\mid_{t_n} - \int_{\hat{S}_i} F(U)\cdot n dS\ , \tag{1.5}$$

when the control volume has a constant face shape $D_i^{n+1} = D_i^n$. In such a case, the complementary boundary surface $\hat{S}_i$ is parallel to the time axis.

The discontinuities of the numerical solution u form an *INTERFACE* (set of *POINTs* for a 1D ambient dimensional space, *CURVEs* for 2D, and *SURFACEs* for 3D), which is propagated from one time level to the next. These interface constituents are described in a piecewise linear manner, and made up of linear elements (simplexes), which are defined by their vertices, the interface *POINTs*. The front *POINTs* are propagated by solving the Riemann Problem in the normal direction and a tangential sweep to update the states on the interface. Here and below, we use the dimension D of an interface to refer to the ambient space in which it is embedded. Thus D may be the dimension of space or of space time, and the elements of the D dimensional interface have intrinsic dimension D - 1 (co-dimension 1) or lower. See [18–20] for details.

The conservative front tracking algorithm contains the following major steps:

1. To propagate the spatial interface at time level n to a new interface at time level $n + 1$. The grid-free interface, or its LGB reconstruction in the case of spatial tangles, is the permanent interface used within the time step propagation loop, while the space-time GB interface is only used for

the space-time control volume reconstruction. While the clipping of the grid-free interface to become grid-based introduces a truncation error at each time step, this error is not involved in the interface propagation to subsequent time steps.

2. To construct the space-time interface by joining two spatial interfaces at time level n and $n+1$. Given two piecewise linear spatial *INTERFACEs* which are separated in time by a step $\triangle t$, we construct (triangulate) a space-time surface joining the two spatial *INTERFACEs*. To construct the space-time interface we perform the following two major tasks for every space-time cell: (1) Construct a grid-free space-time interface by joining the interface at time step n and the new propagated grid free interface at time step $n+1$; (2) Reconstruct the control volume by the convex hull method using the vertices of the grid based space-time interface and corners of the regular space-time control volume.

3. To construct space-time control volumes by using the intersection points of the space-time interface and the space-time cell edges. Those control volumes with small or no top will be merged with their neighboring volumes to satisfy the CFL condition.

4. To use a higher order Godunov type finite volume scheme as in to update the states.

By joining the spatial interfaces at time level n and $n+1$, we construct a space-time manifold which is called the space-time interface. The space-time interface cuts the space-time grid cells into fragments when the grid cell and the

interface intersect. These fragments together with the regular space time grid cells which do not meet the interface are the space-time control volumes. We apply the finite volume scheme to them to calculate the numerical solutions.

The LGB (GF when there is no topological bifurcation) propagated interface poses a difficult problem to the construction of irregular control volume. Therefore, to simplify the procedure of constructing space-time control volume $\{\mathcal{V}_i\}$ in (1.4), we clip the GF space-time interface into a GB space-time interface. As a result, the space-time control volumes are grid based and their vertices are intersections of the space-time interface and regular space-time cell edges.

1.3 Dissertation Organization

Chapter 1 first gives the overview and brief review of the front tracking and fully conservative front tracking method.

Chapter 2 present the governing equation and the numerical development for LES with turbulence models.

In Chapter 3 we describe the test problem setup and our goal. We explore mesh refinement and mesh convergence and dependence on a range of Reynolds numbers.

In Chapter 4 and 5, we present microscopic and macroscopic aspects of mixing. Specializing to a 2D circular RM flow, we find sensitivities to numerical and physical modeling for macroscopic variables and microscopic variables. The interface length depends sensitively on the numerical and physical modeling. Consequently, interface sensitive quantities such as mass diffusion and

atomic level mixing have a similar dependence. We also observe that macroscopic variables are insensitive to variation of physical and numerical modeling while the microscopic variables are highly sensitive.

Chapter 6 discusses the mathematical existence and uniqueness theories and the conclusion is discussed in Chapter 7.

Chapter 2

Developments for LES with turbulence models

The governing equation and the numerical development for LES are presented in this chapter.

2.1 The Governing Equations

We study the compressible Navier-Stokes equations with viscosity, mass diffusion and thermal conductivity, for two miscible species initially separated by a sharp interface. The primitive equations describe the DNS limit, in which transport effects are resolved. A measure of this limit, as applied to the momentum equation, is the criteria $\lambda_{K\text{mesh}} \geq 1$ where $\lambda_{K\text{mesh}} = \lambda_K/\Delta x$ and λ_K is the Kolmogorov length scale,

$$\lambda_K = (\nu_k^3/\epsilon)^{1/4} \ , \tag{2.1}$$

where

$$\epsilon = \nu_k |\mathbf{S}|^2 \ , \tag{2.2}$$

$\mathbf{S}$ is the strain rate tensor

$$S_{ij} = \frac{1}{2}\left(\frac{\partial v_i}{\partial x_j} + \frac{\partial v_j}{\partial x_i}\right) \tag{2.3}$$

defined in terms of the velocity $\mathbf{v}$ and for any matrix $\mathbf{A} = A_{ij}$,

$$|\mathbf{A}|^2 = \sum 2A_{ij}^2 \ . \tag{2.4}$$

A related convergence measure, but applicable to the concentration and energy equations is that the ratio of the turbulent transport parameters (i.e. the coefficients of the dynamic subgrid scale models (given below)) to the molecular ones be small.

LES start from a filter, or averaging procedure, applied to the primitive equations of compressible flow. We adopt what is known as an implicit filter, namely a grid block average. In this case the quantities in the defining equations are averaged over a grid block. New terms, arising from the average of the nonlinear terms, are introduced into the equations. We use a conventional definition of these terms, following refs.[14, 40, 42]. The subgrid models are parameterized dynamically, meaning that the model parameters are determined completely from the resolved scales. In this sense, the models are parameter free. For DNS, these terms have little effect.

We write the filtered continuity, momentum, energy and concentration equations for two miscible fluid species in an inertial frame. The filtered quantities are considered to be mesh block averages, and denoted with an overbar, while mass averaged quantities are denoted with a tilde. Repeated indices are

summed.

$$\frac{\partial \overline{\rho}}{\partial t} + \frac{\partial \overline{\rho}\widetilde{v_i}}{\partial x_i} = 0 \ , \tag{2.5}$$

$$\frac{\partial \overline{\rho}\widetilde{v_j}}{\partial t} + \frac{\partial(\overline{\rho}\widetilde{v_i}\widetilde{v_j} + \overline{p}\delta_{ij})}{\partial x_i} = \frac{\partial \overline{d_{ij}}}{\partial x_i} - \frac{\partial \tau_{ij}}{\partial x_i} \ , \tag{2.6}$$

$$\frac{\partial \overline{E}}{\partial t} + \frac{\partial(\overline{E} + \overline{p})\widetilde{v_i}}{\partial x_i} \ = \frac{\partial \overline{d_{ij}}\widetilde{v_j}}{\partial x_i} + \frac{\partial}{\partial x_i}\left(\overline{\kappa}\frac{\partial \widetilde{T}}{\partial x_i}\right) + \frac{\partial}{\partial x_i}\left((\widetilde{H_h} - \widetilde{H_l})\overline{\rho}\widetilde{D}\frac{\partial \widetilde{\psi}}{\partial x_i}\right) \tag{2.7}$$

$$+ \left(\frac{1}{2}\frac{\partial \tau_{kk}\widetilde{v_i}}{\partial x_i} - \frac{\partial q_i^{(H)}}{\partial x_i} - \frac{\partial q_i^{(T)}}{\partial x_i} - \frac{\partial q_i^{(V)}}{\partial x_i}\right) \ , \tag{2.8}$$

$$\frac{\partial \overline{\rho}\widetilde{\psi}}{\partial t} + \frac{\partial \overline{\rho}\widetilde{\psi}\widetilde{v_i}}{\partial x_i} = \frac{\partial}{\partial x_i}\left(\overline{\rho}\widetilde{D}\frac{\partial \widetilde{\psi}}{\partial x_i}\right) - \frac{\partial q_i^{(\psi)}}{\partial x_i} \ , \tag{2.9}$$

where the subgrid scale (SGS) variables are the τ_{ij}, $q_i^{(H)}$, $q_i^{(T)}$, $q_i^{(V)}$ and $q_i^{(\psi)}$. They are expressed as

$$\tau_{ij} = \overline{\rho}(\widetilde{v_i v_j} - \widetilde{v_i}\widetilde{v_j}) \tag{2.10}$$

$$q_i^{(H)} = \overline{\rho}(\widetilde{c_p T v_i} - \widetilde{c_p}\widetilde{T}\widetilde{v_i}) \tag{2.11}$$

$$q_i^{(T)} = \frac{1}{2}\overline{\rho}(\widetilde{v_k v_k v_i} - \widetilde{v_k}\widetilde{v_k}\widetilde{v_i}) \tag{2.12}$$

$$q_i^{(V)} = \overline{d_{ij} v_j} - \overline{d_{ij}}\widetilde{v_j} \tag{2.13}$$

$$q_i^{(\psi)} = \overline{\rho}(\widetilde{\psi v_i} - \widetilde{\psi}\widetilde{v_i}) \ . \tag{2.14}$$

The dependent filtered variables $\overline{\rho}$, $\widetilde{\psi}$, $\widetilde{v_i}$, $\overline{p}$ and $\overline{E}$ denote, respectively, the total mass density, the species mass fraction, the velocity, the pressure,

and the total specific energy with

$$\overline{E} = \overline{\rho}\widetilde{e} + \overline{\rho}\widetilde{v_k}^2/2 + \tau_{kk}/2 \ . \tag{2.15}$$

Here $\widetilde{H_h}$ and $\widetilde{H_l}$ are the partial specific enthalpy of each species defined by

$$\widetilde{H_h} = \widetilde{e_h} + \frac{\overline{p}}{\overline{\rho}} \tag{2.16}$$

$$\widetilde{H_l} = \widetilde{e_l} + \frac{\overline{p}}{\overline{\rho}} \ , \tag{2.17}$$

where $\widetilde{e_h}$ and $\widetilde{e_l}$ are the specific internal energy of each species. The equation of state for each of the species is taken to be a stiffened gamma law gas.

For simplicity, we assume that the mixture of the two fluids, at the level of a single grid block not meeting an interface, or for a cut grid block on one side of an interface, is mixed at a molecular level. Thus we do not consider turbulent modeling corrections to the grid level equation of state. The equation of state for a mixture of stiffened polytropic gases is not a stiffened polytropic gas, when the stiffening parameters p_∞ of the two species are unequal. As is conventional, we impose pressure and temperature equilibrium for the grid cell or cut cell mixture. The thermodynamic functions are then given as solutions of an algebraic equation, and for the case to two fluids, as is considered here, the algebraic equation is quadratic, and solvable in closed form.

The viscous stress tensor d_{ij} is expressed as

$$\overline{d_{ij}} = \overline{\nu_d}\left(\left(\frac{\partial\widetilde{v_i}}{\partial x_j} + \frac{\partial\widetilde{v_j}}{\partial x_i}\right) - \frac{2}{3}\frac{\partial\widetilde{v_k}}{\partial x_k}\delta_{ij}\right) \ , \tag{2.18}$$

where $\overline{\nu_d} = \overline{\rho\nu_k}$ is the filtered dynamic viscosity. For simplicity, we take $\overline{\nu_d}$ to be a global constant. A more fundamental theory of multifluid viscosity is described in the book of Williams [56].

To derive the filtered energy equation (2.7), we write

$$\overline{(E+p)v_i} = \overline{\rho e v_i + \frac{1}{2}\rho v_k v_k v_i + p v_i} \tag{2.19}$$

$$= \overline{\rho c_v T v_i + \rho e_\infty v_i + p_\infty v_i + (\gamma-1)\rho c_v T v_i - p_\infty v_i} + \frac{1}{2}\overline{\rho v_k v_k v_i} \tag{2.20}$$

$$= (\overline{\rho}\widetilde{c_v}\widetilde{T}\widetilde{v_i} + \overline{\rho}\widetilde{e_\infty}\widetilde{v_i} + (\widetilde{\gamma}-1)\overline{\rho}\widetilde{c_v}\widetilde{T}\widetilde{v_i} + \overline{p_\infty}\widetilde{v_i} - \overline{p_\infty}\widetilde{v_i}) + \frac{1}{2}\overline{\rho}\widetilde{v_k}\widetilde{v_k}\widetilde{v_i} \tag{2.21}$$

$$+ \overline{\rho}(\widetilde{\gamma c_v T v_i} - \widetilde{\gamma}\widetilde{c_v}\widetilde{T}\widetilde{v_i}) + \overline{\rho}(\widetilde{e_\infty v_i} - \widetilde{e_\infty}\widetilde{v_i}) + \frac{1}{2}\overline{\rho}(\widetilde{v_k v_k v_i} - \widetilde{v_k}\widetilde{v_k}\widetilde{v_i})) \tag{2.22}$$

$$= (\overline{E}+\overline{p})\widetilde{v_i} + (q_i^{(H)} + q_i^{(T)}) - \frac{1}{2}\tau_{kk}\widetilde{v_i} + \overline{\rho}(\widetilde{e_\infty v_i} - \widetilde{e_\infty}\widetilde{v_i})\ . \tag{2.23}$$

We model the unclosed difference $\overline{\rho}(\widetilde{e_\infty v_i} - \widetilde{e_\infty}\widetilde{v_i})$ as zero in (2.23).

2.2 Numerical Development for LES

The parabolic Navier-Stokes equations are solved via operator splitting, with separate solution steps for the hyperbolic and pure diffusion parts of the equations. The hyperbolic solutions are obtained by the front tracking FronTier algorithm [10]. The interface hyperbolic updates are split into normal and tangential operators defined at front points. The normal update uses a predictor-corrector algorithm, with the predictor step a Riemann solution

using the left and right front states as input. The corrector step, based on finite differences in characteristic coordinates, couples the normal direction front propagation to signals coming from interior states. The interior hyperbolic update uses a Godunov finite difference solver based on the MUSCL algorithm [7, 57]. A sharp (tracked) interface in the hyperbolic update uses ghost cells [27] in the interior state update to eliminate [38] transport related numerical mass and thermal diffusion across the interface.

Physical transport for front states is introduced via finite differences in a normal-tangential rectangular coordinate system at the front. Discretization is outlined in Section 2.2.1, where the turbulent transport term is defined. The parabolic update of the interior states, i.e. the inclusion of molecular and turbulent transport terms for species diffusion, viscosity and thermal heat conductivity, is via conventional finite differences. Irregular stencils for the interior states, i.e. the stencils crossing the front, are treated conventionally, without regard to the front or any ghost cell values. An explicit solver for both the interior and the front state parabolic solvers, with possible time step subcycling, is sufficient to allow a stable computation for most of the mesh and transport parameter range considered.

For the highly heat diffusive plasma conditions, an implicit solver is used. With transport terms strong enough to require an implicit solver, there is no need for, or benefit from, tracking. Moreover, the formulation of the tracked front states together with the interior states appears to be inconsistent with common implicit solver algorithms. We allow selective untracking of specific (primitive) variables within an overall tracked solution. In this algorithm, after

the interior and front state updates, the untracked front states (the primitive variables that are not being tracked, for example energy, in the case p) are re-determined by one sided interpolation from neighboring interior states of the same component. Here one sided means that the interpolating interior states are restricted to have the same component as that of the front state in question. In the unusual case of no nearby interior states with the required component, a two sided interpolation is used, in which the component restriction is dropped. As a test of this algorithm, we compared it to two sided interpolation, and we compared it to an explicit algorithm (with tracking of the primitive energy variable). For this case, extensive subcycling in the parabolic step for the energy equation was needed for numerical stability. There was no notable difference among these three algorithms. The FronTier numerical Schmidt and Prandtl numbers are ∞, and the code allows efficient simulation of any desired (physical) Schmidt or Prandtl number.

We develop the subgrid scale dynamic model terms used in this thesis, following and slightly extending ideas of [40, 42].

2.2.1 A Subgrid Scale Dynamic Model for the Momentum Equation

We use the trace-free Smagorinsky eddy viscosity model for the sub grid scale (SGS) stress τ_{ij} . The τ_{ij} can be decomposed into an anisotropic (trace

zero) tensor (τ_{ij}^a) and an isotropic tensor (τ_{ij}^i), which are modeled separately:

$$\tau_{ij}^M = \left(\tau_{ij} - \tau_{kk}\frac{\delta_{ij}}{3}\right) + \tau_{kk}\frac{\delta_{ij}}{3} = \tau_{ij}^a + \tau_{ij}^i = -2C_S\Delta^2\overline{\rho}|\widetilde{S}|\widetilde{S}_{ij}^a + \frac{\delta_{ij}}{3}2C_I\Delta^2\overline{\rho}|\widetilde{S}|^2 \ , \tag{2.24}$$

where $\widetilde{S}_{ij}^a = \widetilde{S}_{ij} - \frac{\delta_{ij}}{3}\widetilde{S}_{kk}$. and $|\cdot|$ is defined by (2.4). The C_S and C_I are model coefficients to be computed dynamically. In analogy to (2.18), we define

$$\nu_{kt} = C_S\Delta^2|\widetilde{S}| \tag{2.25}$$

as the kinematic turbulent viscosity.

The key element of the dynamic model is the utilization of the data contained in the resolved field. This information is brought to bear by introducing a test filter with a larger filter width $\widehat{\Delta}$ than the resolved grid filter. We will use a 2×2 mesh block average to define the test filter. Let a spatially test-filtered quantity be denoted by a caret. The test filtered stress T_{ij} is defined as:

$$T_{ij} = \widehat{\overline{\rho v_i v_j}} - \frac{\widehat{\overline{\rho v_i}}\ \widehat{\overline{\rho v_j}}}{\widehat{\overline{\rho}}} \tag{2.26}$$

and is modeled as:

$$T_{ij}^M = T_{ij}^a + T_{ij}^i = -2C_S\widehat{\Delta}^2\widehat{\overline{\rho}}|\widehat{\widetilde{S}}|\widehat{\widetilde{S}}_{ij}^a + \frac{2\delta_{ij}}{3}C_I\widehat{\Delta}^2\widehat{\overline{\rho}}|\widehat{\widetilde{S}}|^2 \ . \tag{2.27}$$

Using Germano's identity [14], the Leonard stress L_{ij} can be expressed

as:

$$L_{ij} = T_{ij} - \widehat{\tau_{ij}} = \widehat{\left(\frac{\overline{\rho v_i}\,\overline{\rho v_j}}{\overline{\rho}}\right)} - \frac{\widehat{\overline{\rho v_i}}\,\widehat{\overline{\rho v_j}}}{\widehat{\overline{\rho}}} = \widehat{\overline{\rho}\widetilde{v}_i\widetilde{v}_j} - \frac{\widehat{\overline{\rho}\widetilde{v}_i}\widehat{\overline{\rho}\widetilde{v}_j}}{\widehat{\overline{\rho}}} \ . \tag{2.28}$$

The right hand side is completely computable from the resolved variables. We next introduce the ansatz that C_S and C_I are independent of the length scale. In other words, the same C_S and C_I occur in (2.24) and (2.27). In this case,

$$L^a_{ij} = T^a_{ij} - \widehat{\tau}^a_{ij} = 2C_S\Delta^2\widehat{\overline{\rho}|\widetilde{S}|\widetilde{S}_{ij}} - 2C_S\widehat{\Delta}^2\widehat{\overline{\rho}}|\widehat{\widetilde{S}}|\widehat{\widetilde{S}}^a_{ij} = C_S M^a_{ij} \ , \tag{2.29}$$

where

$$M^a_{ij} = 2\Delta^2\widehat{\overline{\rho}|\widetilde{S}|\widetilde{S}_{ij}} - 2\widehat{\Delta}^2\widehat{\overline{\rho}}|\widehat{\widetilde{S}}|\widehat{\widetilde{S}}^a_{ij} \ . \tag{2.30}$$

We would next solve (2.29) for C_S. However, this equation corresponds to five independent relations for C_S and an algebraic solution is not possible.

We introduce an averaging operation $\langle\cdots\rangle$. The specification of the average is problem dependent, as the universal definition of an ensemble average is inconvenient to use. For the present problem, we regard this average as taken over the symmetry variable θ, i.e., an average over circular arcs (constant radius). To assure numerical regularity, we also apply a convolution average in the radial direction with a stencil extending $\pm 6\Delta r$ from current radius.

Applying this average to (2.29) and using least squares in the resulting

equations leads to the formula

$$C_S = \frac{\langle (\sum L_{ij}^a M_{ij}^a)^+ \rangle}{\langle (\sum M_{ij}^a M_{ij}^a)^+ \rangle} \ . \tag{2.31}$$

Here the expression $(\cdots)^+$ means the positive part of the quantity in the parenthesis. In other words, we clip negative values. This step is consistent with methods proposed elsewhere [40]. The same method is used for the coefficients of turbulent heat conduction and species concentration diffusion.

The turbulent viscosity determined by (2.31) and the related turbulent transport coefficients determined below were monitored for the simulations of the present study. The results were generally consistent with theoretical expectations. For example, the turbulent viscosity was respectively small (comparable, dominant) in relation to the molecular value of viscosity for the three cases of DNS, LES near to DNS, and LES far from DNS.

To determine C_I, we consider

$$L_{kk}^i = T_{kk}^i - \widehat{\tau}_{kk}^i = -2C_I \Delta^2 \widehat{\overline{\rho}|\widetilde{S}|^2} + 2C_I \widehat{\Delta}^2 \widehat{\overline{\rho}} |\widehat{\widetilde{S}}|^2 = C_I M_{kk}^i \ , \tag{2.32}$$

where a summation convention was used for the kk repeated indices and

$$M_{kk}^i = -2\Delta^2 \widehat{\overline{\rho}|\widetilde{S}|^2} + 2\widehat{\Delta}^2 \widehat{\overline{\rho}} |\widehat{\widetilde{S}}|^2 \tag{2.33}$$

This equation corresponds to one relation for C_I, from which we obtain

$$C_I = \frac{\langle L_{kk}^i \rangle}{\langle M_{kk}^i \rangle} \ . \tag{2.34}$$

To discretize the elliptic operators associated with the molecular level and subgrid scale transport terms, we use the same stencil at each front point that was used in the front propagation. This stencil is rectilinear, and aligned with the normal and tangential directions to the front at the front point in question. We use three mesh points in each of the normal and the tangential directions. Letting ∂_N and ∂_T denote derivatives in the normal and tangential directions, we first write the discretization for $\partial_N c \partial_N f$ for some function f and spatially dependent coefficient c. The function is double valued at the front, and so we specify, as an example, a discretization of the left value, f_l. The discrete operator has the form

$$c_{+1/2}(f_+ - f_{0l}) - c_{-1/2}(f_{0l} - f_-) = c_{+1/2} f_+ - (c_{+1/2} + c_{-1/2}) f_{0l} + c_{-1/2} f_- \ . \quad (2.35)$$

Here f_{0l} and f_{0r} are front states on the left and right side of the front, while $f_\pm$ and $c_{\pm 1/2}$ are evaluated along the normal to the front at distances $\pm \Delta x$ or $\pm 1/2 \ \Delta x$ from the front.

The normal direction discretization for the right front state is similar, and the tangential direction discretizations differ only in that all values are associated with either the left or the right side of the front.

The discretization of the mixed partials is complicated by the use of a 5 point stencil and a fixed order of differentiation. We write

$$\partial_N c \partial_T f = \partial_T c \partial_N f + (\partial_N c)(\partial_T f) - (\partial_T c)(\partial_N f) \ . \quad (2.36)$$

The normal sweep is performed in advance of the tangential sweep. Use of

(2.36) allows all mixed partial derivatives to be evaluated in the order of the sweeps, first normal derivatives and then tangential derivatives. During the normal sweep, we evaluate and store front values for $\partial_N c$ and $\partial_N f$, which can be differenced using obvious formulas during the tangential sweep to yield a discrete expression for the LHS of (2.36).

2.2.2 A Subgrid Scale Dynamic Model for the Energy Equation

We only consider the eddy diffusivity SGS model for the SGS heat transport flux $q_i^{(H)}$ with some modeling assumptions (e.g. negligible subgrid viscous work and triple correlations). As in ref. [30], we set $q_i^{(T)} = 0 = q_i^{(V)}$. The SGS heat transport flux is modeled as:

$$q_i^{(H)M} = -\overline{\rho}\widetilde{c_p}\frac{C_S\Delta^2|\widetilde{S}|}{Pr_t}\frac{\partial\widetilde{T}}{\partial x_i} \tag{2.37}$$

$$= -\overline{\rho}\widetilde{c_p}\frac{\nu_{kt}}{Pr_t}\frac{\partial\widetilde{T}}{\partial x_i}\ , \tag{2.38}$$

where Pr_t is the SGS turbulent Prandtl number to be determined using a dynamic model.

At the test filter level, the flux is defined as:

$$Q_i^{(H)} = \widehat{\overline{\rho c_p T v_i}} - \frac{\widehat{\overline{\rho c_p}}\ \widehat{\overline{\rho T}}\ \widehat{\overline{\rho v_i}}}{\widehat{\overline{\rho}}^2}\ , \tag{2.39}$$

and is modeled as:

$$Q_i^{(H)M} = -\widehat{\overline{\rho}}\widehat{\widetilde{c_p}}\frac{C_S\widehat{\Delta}^2|\widehat{\widetilde{S}}|}{Pr_t}\frac{\partial\widehat{\widetilde{T}}}{\partial x_i} \ . \tag{2.40}$$

Again, using Germano's identity, we have

$$L_i^{(H)} = Q_i^{(H)} - \widehat{q_i^{(H)}} = \left(\frac{\widehat{\overline{\rho c_p}\ \overline{\rho T}\overline{\rho v_i}}}{\overline{\rho}^2}\right) - \frac{\widehat{\overline{\rho c_p}}\widehat{\overline{\rho T}}\widehat{\overline{\rho v_i}}}{\widehat{\overline{\rho}}^2} = \widehat{\overline{\rho}\widetilde{c_p}\widetilde{T}\widetilde{v_i}} - \frac{\widehat{\overline{\rho}\widetilde{c_p}}\widehat{\overline{\rho}\widetilde{T}}\widehat{\overline{\rho}\widetilde{v_i}}}{\widehat{\overline{\rho}}^2} \ . \tag{2.41}$$

To determine Pr_t,

$$L_i^{(H)} = Q_i^{(H)M} - \widehat{q_i^{(H)M}} = \frac{C_S}{Pr_t}\left(\Delta^2\left(\widehat{\overline{\rho}\widetilde{c_p}|\widetilde{S}|\frac{\partial\widetilde{T}}{\partial x_i}}\right) - \widehat{\Delta}^2\widehat{\overline{\rho}}\widehat{\widetilde{c_p}}|\widehat{\widetilde{S}}|\frac{\partial\widehat{\widetilde{T}}}{\partial x_i}\right) = \frac{C_S}{Pr_t}M_i^{(H)} \ , \tag{2.42}$$

where

$$M_i^{(H)} = \Delta^2\left(\widehat{\overline{\rho}\widetilde{c_p}|\widetilde{S}|\frac{\partial\widetilde{T}}{\partial x_i}}\right) - \widehat{\Delta}^2\widehat{\overline{\rho}}\widehat{\widetilde{c_p}}|\widehat{\widetilde{S}}|\frac{\partial\widehat{\widetilde{T}}}{\partial x_i} \ . \tag{2.43}$$

This equation corresponds to three independent relations and again a least square approach is followed to calculate the model coefficient,

$$Pr_t = C_S\frac{\langle(\sum M_i^{(H)}M_i^{(H)})^+\rangle}{\langle(\sum L_i^{(H)}M_i^{(H)})^+\rangle} \ . \tag{2.44}$$

Discretization is as in (2.35).

2.2.3 A Subgrid Scale Dynamic Model for the Concentration Equation

For SGS scalar transport, from a gradient transport modeling assumption,

$$q_i^{(\psi)M} = -\overline{\rho}\frac{C_S\Delta^2|\widetilde{S}|}{Sc_t}\frac{\partial\widetilde{\psi}}{\partial x_i} = -\overline{\rho}\frac{\nu_{kt}}{Sc_t}\frac{\partial\widetilde{\psi}}{\partial x_i} \ , \tag{2.45}$$

where Sc_t is the SGS turbulent Schmidt number to be determined using a dynamic model.

At the test filter level, the SGS scalar transport is defined as:

$$Q_i^{(\psi)} = \widehat{\overline{\rho v_i}\psi} - \frac{\widehat{\overline{\rho v_i}}\,\widehat{\overline{\rho\psi}}}{\widehat{\overline{\rho}}} \ , \tag{2.46}$$

and is modeled as:

$$Q_i^{(\psi)M} = -\widehat{\overline{\rho}}\frac{C_S\widehat{\Delta}^2|\widehat{\widetilde{S}}|}{Sc_t}\frac{\partial\widehat{\widetilde{\psi}}}{\partial x_i} \ . \tag{2.47}$$

Using Germano's identity, we have

$$L_i^{\psi} = Q_i^{(\psi)} - \widehat{q_i^{(\psi)}} = \left(\frac{\widehat{\overline{\rho v_i}}\,\widehat{\overline{\rho\psi}}}{\overline{\rho}}\right) - \frac{\widehat{\overline{\rho v_i}}\,\widehat{\overline{\rho\psi}}}{\widehat{\overline{\rho}}} = \widehat{\overline{\rho}\widetilde{v}_i\widetilde{\psi}} - \frac{\widehat{\overline{\rho}\widetilde{v}_i}\,\widehat{\overline{\rho}\widetilde{\psi}}}{\widehat{\overline{\rho}}} \ . \tag{2.48}$$

To determine Sc_t,

$$L_i^{\psi} = Q_i^{(\psi)M} - \widehat{q_i^{(\psi)M}} = \frac{C_S}{Sc_t}\left(\Delta^2\left(\widehat{\overline{\rho}|\widetilde{S}|\frac{\partial\widetilde{\psi}}{\partial x_i}}\right) - \widehat{\Delta}^2\widehat{\overline{\rho}}|\widehat{\widetilde{S}}|\frac{\partial\widehat{\widetilde{\psi}}}{\partial x_i}\right) = \frac{C_S}{Sc_t}M_i^{(\psi)} \ , \tag{2.49}$$

where

$$M_i^{(\psi)} = \Delta^2\left(\widehat{\overline{\rho}|\widetilde{S}|\frac{\partial\widetilde{\psi}}{\partial x_i}}\right) - \widehat{\Delta}^2\widehat{\overline{\rho}}|\widehat{\widetilde{S}}|\frac{\partial\widehat{\widetilde{\psi}}}{\partial x_i} \ . \tag{2.50}$$

This equation corresponds to three independent relations. Again, a least square approach is followed to calculate the model coefficient,

$$Sc_t = C_S\frac{\langle(\sum M_i^{(\psi)}M_i^{(\psi)})^+\rangle}{\langle(\sum L_i^{(\psi)}M_i^{(\psi)})^+\rangle} \ . \tag{2.51}$$

Chapter 3

The Flow Instability Problem

The turbulent mixing considered here is initiated by a shock wave passing through a layer separating two fluids of distinct densities. When the layer is perturbed (or not normal relative to the shock wave), vorticity is deposited on the interface by the shock passage. This vorticity causes the interface to roll up and become unstable. Upon passage of a second shock wave, the interface enters an extremely chaotic regime. This is an example of a Richtmyer-Meshkov (RM) instability.

We consider a circular geometry, with a converging circular shock at the outer edge, and inside this, two fluids separated by a perturbed circular interface. The chaotic aspects of the mixing at a molecular level following reshock challenge some conventional ideas of computational science while supporting others. For this reason, the problem is of fundamental scientific interest, and may shed light on differing views for the computation of turbulent mixing flows.

3.1 Test Problem Setup

We consider a computational domain $x, y \in [0, 25] \times [-25, 25]$ (units of cm). Time units are in micro seconds, and pressure is in Megabars. With r denoting the radial coordinate in the x, y plane, the initial contact is perturbed from a circle at $r = 12.5$. Outside this contact is a stiffened gamma law gas, with parameters given by $\gamma = 3.27$, $p_\infty = 0.1495$, $e_\infty = 1.25 \times 10^{-18}$ and $c_v = 2.2 \times 10^{-6}$, where the stiffened gamma law gas is defined by

$$e + e_\infty = c_v T + \frac{p_\infty}{\rho} \tag{3.1}$$

and

$$p + p_\infty = (\gamma - 1)\rho c_v T. \tag{3.2}$$

Here, γ is the adiabatic exponent and c_v is the specific heat at constant volume and e_∞ is the energy of formation and p_∞ has the dimensions of a pressure. Inside the contact is also a stiffened gamma law gas, representing lucite, with parameters $\gamma = 1.85$, $p_\infty = 0.03036$, $e_\infty = 2.49 \times 10^{-18}$ and $c_v = 1.46 \times 10^{-5}$. The time dependent boundary condition from the RAGE code [41] is located at $r = 24$. The initial ambient pressure is $p = 10^{-6}$, and the initial pressure at the boundary is $p = 0.02648$, giving rise to an inward propagating shock at $t = 0$. The heavy fluid density is 7.282 and the light fluid density is 1.182, giving an Atwood number $A = 0.72$. Initial and late time simulation density plots of unregularized simulations (zero transport coefficients) are shown in Fig. 3.1.

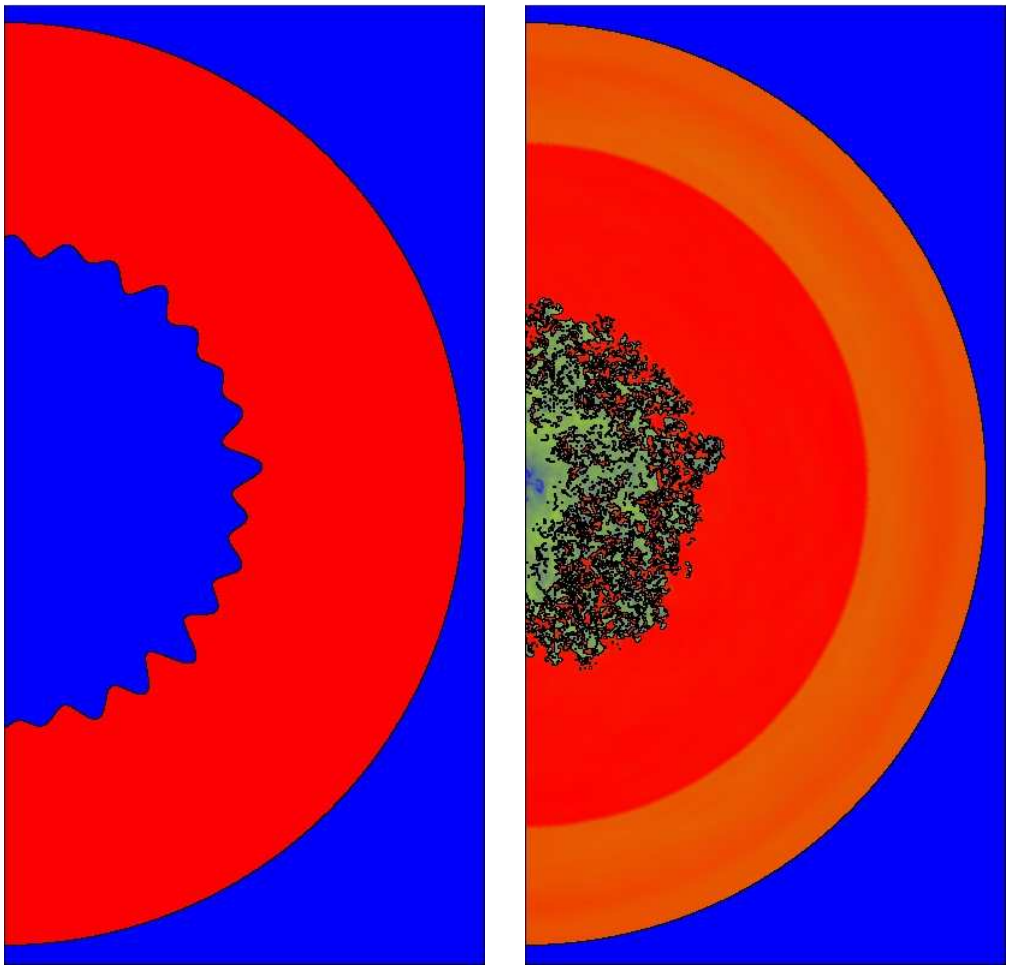

Figure 3.1: Initial (left) and late time (right) density plot for the Richtmyer-Meshkov fluid instability (unregularized, with zero physical transport coefficients) under study in this paper.

In the problem considered here, the flow is dominated by a single strong shock wave, starting at the outer edge of the computational domain (a half circle). The shock passes through the interface separating the two fluids, proceeds to the origin, reflects there and expands outward, recrossing the interface region and finally exiting at the outer boundary. The interface between the two fluids is defined as a 50% iso-concentration contour.

Due to the shock induced instability, the interface region expands into a mixing zone, which has a very complex structure. Especially after the second passage of the shock (the reshock or reflected shock passage), the mixing zone becomes highly chaotic. The inner and outer edges of the mixing zone are defined in terms of 5% and 95% volume fraction contours, after a spatial average over the circular symmetry variable. The mixing zone is then defined as the region between these inner and outer edges. The software which captures the space time trajectory of these waves in the numerical solution is known as a wave filter [11, 16, 59]. A space time plot of the shock trajectories and mixing zone edges is shown in Fig. 3.2.

We have already observed [33] that the interface for the problem under study is chaotic, with length proportional to Δx^{-1}, with respect to its mesh (non) convergence (i.e. rate of divergence) properties. This fact is demonstrated in Fig. 3.3, where the length / area ratio is shown in physical units (left frame) and mesh units (right frame); transport coefficients have been set to zero.

From Fig. 3.3, we observe that somewhat after reshock, the interface length, in mesh units, occupies a constant ratio to the mesh area of the mixing

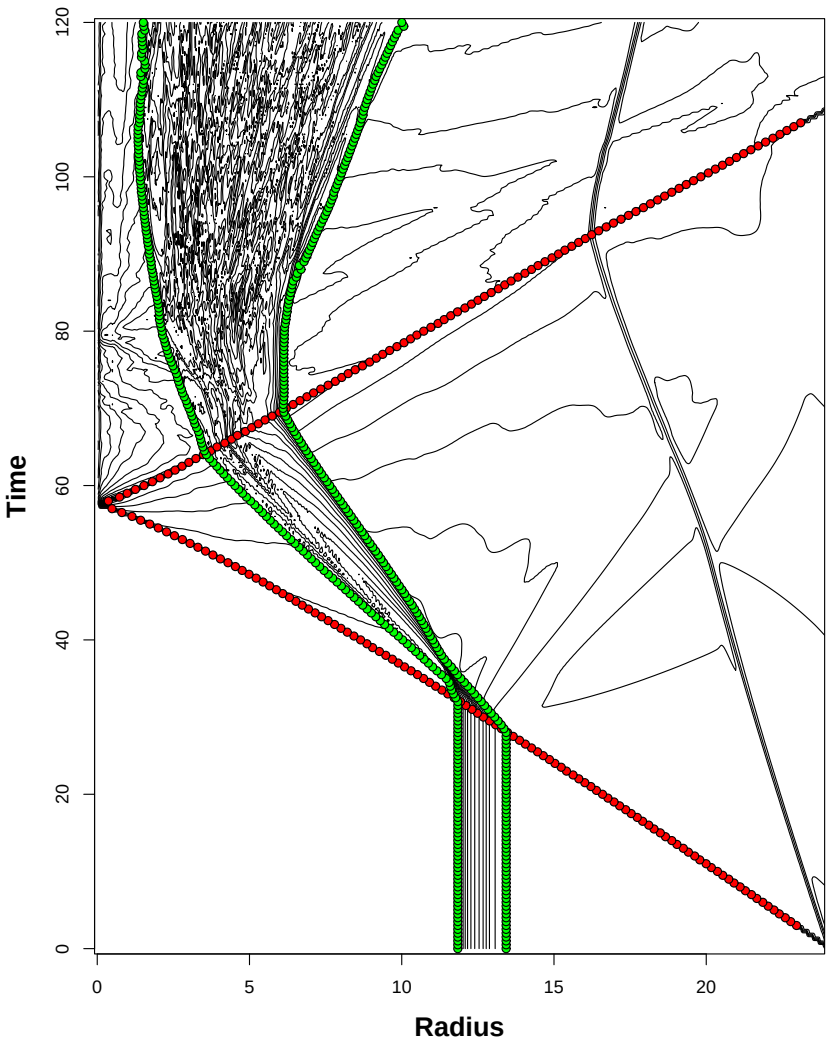

Figure 3.2: Space time (r, t) contours of the primary waves, as detected by the wave filter algorithm. These are the inward (direct) and outward (reflected) shock waves and the inner and outer edges of the mixing zone, all detected within a single rotational averaging window, in this case $\theta \in [-45^o, 0^o]$.

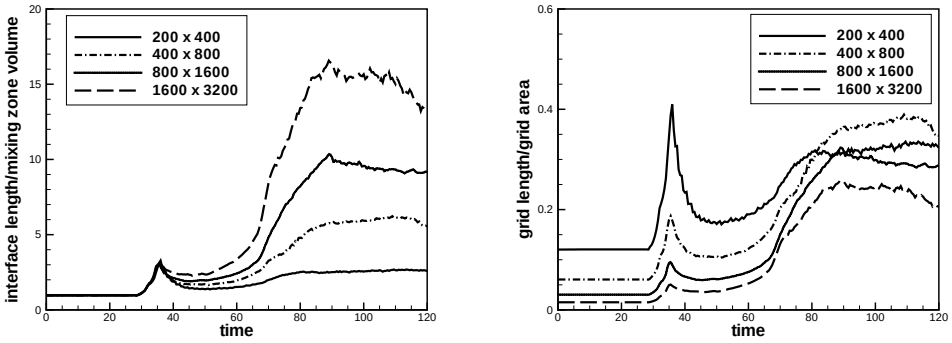

Figure 3.3: Plot of the interface length divided by the mixing zone area vs. time. Left: Length and volume measured in physical units. Right: Length and volume measured in mesh units ([physical length / physical area] $\times\Delta x$). Results for four mesh levels are displayed.

zone. We call this ratio the mesh level surface fraction. Its value is approximately time independent (about 30%), after a transient period following the second shock passage. We note here and in many later plots, some lost of mesh level complexity in the finest grid simulations. Further mesh refinement studies will be needed to determine the evolution of mesh level complexity under continued mesh refinement. In any case, at the grid levels attained here, the interface is mesh volume filling, cutoff by the mesh, and highly complex or chaotic in nature.

3.2 Research Objectives

Our goal is accurate numerical solutions using feasible grids. For the purpose, we verify the use of large eddy simulations (LES). We study mesh refinement and mesh convergence and dependence on a range of Reynolds numbers, including some within the regime of direct numerical simulation

(DNS), in which transport properties are fully resolved.

The fluid interface, at late time, is volume filling. The Reynolds number and transport coefficients (viscosity, mass diffusion, and heat conductivity) are given dimensionlessly as $Re = UL/\nu_k$, the Schmidt number $Sc = \nu_k/D$, and the Prandtl number $Pr = \nu_k/\alpha$. Here ν_k is the kinematic viscosity, D the kinematic mass diffusivity and $\alpha = \frac{\kappa}{\rho c_p}$ the kinematic thermal diffusion rate. κ is the heat conductivity, ρ the density and c_p the specific heat at constant pressure. U and L are characteristic velocity and length scales. Gases typically have Schmidt and Prandtl numbers of the order of unity, while liquids typically have Schmidt numbers in the range $Sc \sim 4 \times 10^2$ to 10^4 and Prandtl numbers in the range $Pr \sim 10$ to 10^2 [1, 48]. Dense plasma transport coefficients have been estimated as $Sc \sim 0.6$ to 1.5 [52] for a range of plasma conditions relevant to NIF experiments. Plasma Prandtl numbers are dependent on ionization levels, nuclear charge, and temperature. A representative plasma value $Pr \sim 10^{-4}$ can be inferred from the viscosity and heat conductivity values quoted by Drake [9]. The very high level of thermal conductivity reflected in this value results from the transport of free electrons, and a time scale sufficient for the thermalization that allows a single temperature description of the plasma. We make no comments on this time scale. Numerical Schmidt and Prandtl numbers are generally not documented. If we assume a numerical shock width of $1.5\Delta x$ and a numerical contact width of $5\Delta x$ for untracked simulations, numerical transport coefficients in the range of 0.3 would be reasonable. On this basis, we consider the transport cases l, g, p from Table 3.1. We allow physical parameters (Re, Sc, Pr) to vary by three orders of magnitude, and

Table 3.1: Transport coefficients considered in this paper, arranged in order of increasing diffusivity. The presumed typical numerical transport parameters are shown for reference only and are not explored here.

case	Schmidt	Prandtl
l (liquid)	10^3	50
g (gas)	1	1
n (numerical)	0.3	0.3
p (plasma)	1	10^{-4}

explore mesh refinement up to 3200 zones per linear dimension. To keep the computational burden manageable, we restrict the simulations to 2D and we restrict the 2D mesh resolution to the finest resolution presently used for 3D simulations.

The emphasis on the joint probability distribution function (pdf) of concentration and temperature as micro scale observables is motivated by problems in turbulent combustion [47], where these variables affect the local flame speed and the overall flow.

The subgrid models are not original here, but their use in flow simulations having numerically sharp gradients appears to be new. In this sense, we are outside of the known domain of validity of the subgrid models, and the present work serves as a verification (i.e. mesh convergence with full resolution of the momentum equation) study.

At least for the present problem, with its somewhat modest number of initial modes, the joint pdf for concentration and temperature are subject to statistical fluctuations. In other words, the spatial averaging over the mixing zone is not sufficient to obtain statistical convergence, and an ensemble of

simulations would be needed to obtain statistically converged mixing statistics. This can be observed from Fig. 3.1, where we see a significant variation in the size of the coherent mixing structures, and a relatively small sample of the larger sized ones, whose size appears to reflect the $t = 0$ perturbation wave length. For this reason, we wish to introduce some degree of averaging into our analysis of the pdfs. Looking to the various applications in which turbulent mixing plays a role, chemical reactions stand out. We are involved in combustion modeling for scram jet design, type Ia supernova studies, and ICF motivated studies. Accordingly, we consider the chemical reaction rate w of a hypothetical reaction $A + B \rightarrow C$ with a hypothetical activation temperature T_{AC} to assess convergence of the pdfs. The coefficient of variation of w, in its dependence on space at fixed time within the mixing zone, is generally over 100%. Thus spatial averaging is needed.

With this definition of spatially averaged convergence, the statistical fluctuations are reduced but not eliminated. We present (as error bars in plots) the fluctuations ($\pm 2\sigma$) associated with variation across an ensemble of sparially averaged quantities. We adopt a pdf for the (single realization) reaction rate values w, with a probability measure $dP(w)$. Then $1 = \int dP(w)$ and the spatial average of w is $\langle w \rangle = \int w dP(w)$. We introduce the notation $dP^x(w)$, $x = c,\ m,\ f$ for the w-pdf for the coarse, medium and fine grids. Then we define the relative error as $\int w|dP^c(w) - dP^f(w)|/\langle w^f \rangle$ for the coarse to fine error, and similarly for the medium to fine error. These continuum expressions are interpreted in terms of binning the data, generally into 10 bins per variable. We observe mesh convergence. Other definitions of convergence give

similar results, except that when the error is well below the level of ensemble variability (realization to realization variation), convergence may be obscured by chance cancellations giving unrealistically small net error on coarse grids. The error definition chosen minimizes such cancellations.

To summarize, the main goal of this paper is to introduce and verify parameterized subgrid models for turbulent mass, momentum and thermal diffusion which will capture unresolved diffusive phenomena as it impacts coarse grid scales in a LES having steep numerical gradients. In this way, we plan to achieve LES which are converging relative to both the macro and the micro observables mentioned above. The simulations are more efficient than those of conventional turbulence models in the narrow width in mesh units that they allow for sharp gradient concentration transitions. They model turbulent transport with microscopic observables correctly computed, in contrast to many capturing simulations. These subgrid models are applied here in a new context, namely to a front tracking and shock capturing Godunov scheme which maintains sharp gradients.

The front tracking code FronTier can achieve arbitrarily high Schmidt and Prandtl numbers numerically without a requirement for mesh refinement beyond that needed to resolve the momentum equation. This is not the case for most (untracked) simulation codes. Numerical mass and thermal diffusion arises primarily within the Eulerian hyperbolic step, due to solution averaging over grid blocks associated with transport by a nonzero velocity field (i.e. hyperbolic transport). This apparently universal feature of untracked Eulerian conservative capturing codes is circumvented with front tracking. Subgrid

models can only add diffusion, and can never remove it. In this sense, a subgrid model for mass or thermal diffusion cannot cure the problem of excess numerical diffusion to achieve accurate modeling of atomic scale mixing. A conventional untracked code must be run in an "over resolved" mode, with more resolution than the momentum equation requires, to achieve low levels of numerical mass or thermal diffusion in the concentration and energy equations. In other words, conventional untracked codes require that the simulations be resolved or convergent in terms of the continuity, species and energy equations as well as for the momentum equation. The use of front tracking, however, avoids or reduces numerical diffusion in the species, continuity, and energy equations, even for coarse grids, and thus requires DNS or LES type convergence of the momentum equation alone.

We also point to the conclusions of Chapter. 4, in which the macro variables (mixing zone edge positions, shock trajectories, etc.) are insensitive to physical or numerical modeling issues, and thus presumably to the choice of the subgrid model for viscosity, or to the viscosity and Reynolds number itself. Thus our convergence studies will focus primarily on the micro variables: the joint pdfs for species concentration and temperature and on a typical chemical reaction rate. We will examine the degree to which these are insensitive to Reynolds number for LES, and to mesh for a fixed Reynolds number LES.

There is a large literature concerning turbulent mixing in RM unstable flows. Most of this literature focuses on macro observables, such as the mixing zone edges and shock trajectories. For RM mixing, these macro observables are insensitive, in that we find generically agreement among theory, experiment

and numerics, cf. [31].

The micro observables (e.g. joint temperature and species PDFs) have received relatively less attention, but we can cite a previous study [30], with conclusions distinct from ours, for a different RM flow. Among experimental studies of micro observables for RM instabilities, we mention two studies of related but distinct flow problems [32, 55]. These experimental studies appear to be qualitatively consistent with our conclusions regarding the mixing, when compared at comparable times and Schmidt numbers. Quoting [32], "Schmidt number plays a role in turbulent mixing of high-Reynolds flows".

The critical dependence of molecular levels of mixing on physical transport (and for under resolved capturing simulations, on numerical transport) is illustrated in Fig. 3.4. This dependence is one of the central points of this thesis.

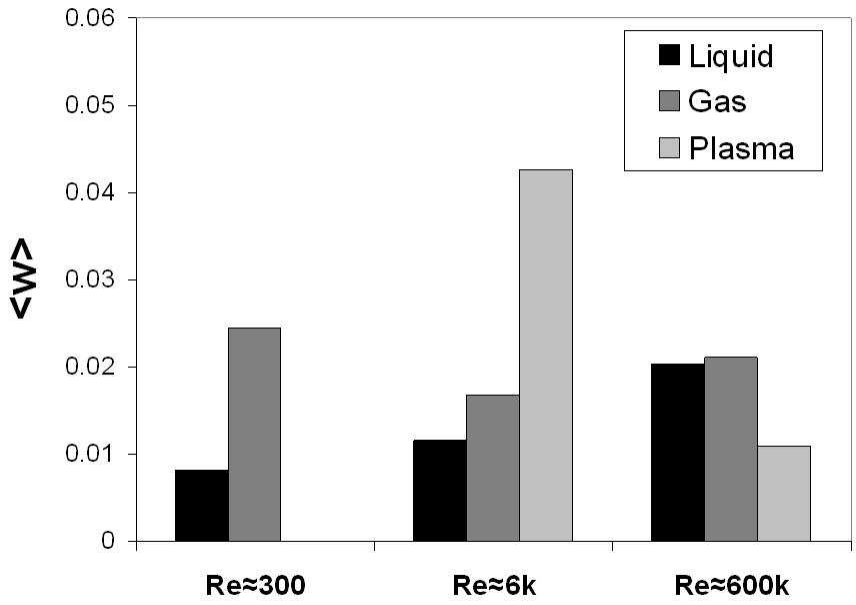

Figure 3.4: Chemical reaction rate at $t = 90$ for three representative values for the transport parameters, and each for three values of the Reynolds number. The activation temperature is chosen as $15,000^oK$. The point of this plot is the strikingly different values obtained for $\langle w \rangle$ for the nine physical regimes considered here.

Chapter 4

Mesh Convergence for Macro Observables

We define a (time dependent) length scale L to be the width of the mixing zone, and the velocity scale U to be the turbulent velocity $U = \sqrt{\langle \delta v^2 \rangle}$. The angle brackets $\langle \cdots \rangle$ denote a spatial avergae over the mixing zone. We observe below that ensemble averages are also relevant. We define $\delta v = v - \langle v \rangle$. We also define $Re_{\text{mesh}} = U \Delta x / \nu_k$.

The objective of the present chapter is to compute the large scale solution features accurately. This includes the trajectories of the principal waves, as illustrated in Fig. 3.2. This objective is related to a systematic convergence study [34, 59]. In that study, we found statistical convergence for many mean flow variables, which define what we call the macroscopic description of the flow. In Fig. 4.1, we plot the time integrated relative wave discrepancy defined in terms of the mixing zone edge positions for a variety of mesh levels and for transport coefficients from Table 3.1. Similar convergence properties have been obtained for other macro variable solution errors such as the mean densities and velocities for each phase. The error (or discrepancy) is deter-

mined by comparison of the simulation to a fine grid (3200×1600) simulation having zero transport coefficients. The reported discrepancy is thus a mixture of mesh errors and discrepancies associated with modification of the transport coefficients from a nominal value (zero). From Fig. 4.1, and related studies [34, 41, 59] we conclude that the macro observables are insensitive to both numerical and physical parameters, except for case p with low Re (large transport parameters).

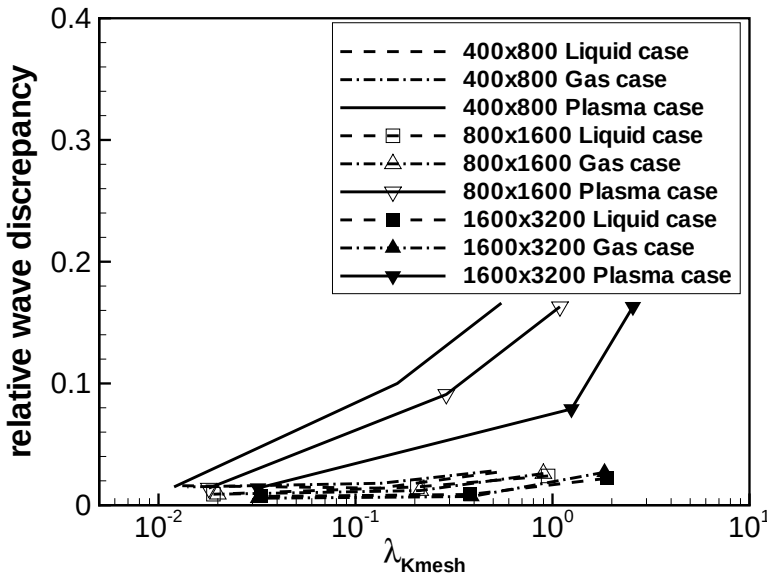

Figure 4.1: Time integrated relative discrepancy in the mixing zone edge locations as compared to a fine grid, zero transport simulation. The discrepancy, for cases l and g, is mainly due to mesh errors and is partly due to modification of physical parameters. The discrepancy decreases with mesh refinement, uniformly as physical parameters are varied. The plasma case p shows convergence, but to a Reynolds number dependent limit distinct (for small Re) from the zero transport case.

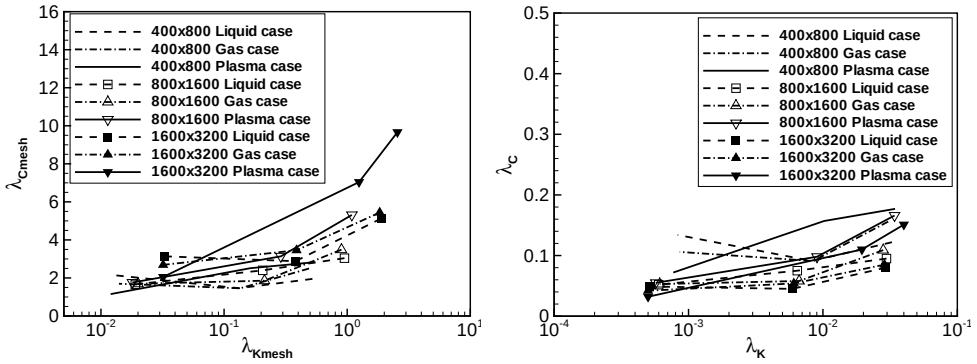

Figure 4.2: Left: plot of $\lambda_C/\Delta x$ vs. $\lambda_{K\text{mesh}}$ for a range of mesh levels and transport parameters cases l, g, p from Table 3.1, at $t = 90$, $r = r_{\text{mid}}$. Right: the same data replotted as λ_C vs. λ_K.

4.1 Correlation and Diffusion Length Scales

We introduce a correlation length scale λ_C to characterize the microstructure of mix. The correlation length is defined in terms of the probability of exit distance ξ from a given phase or mean distance to the complementary phase, introduced [49, 50] for models of opacity, and studied [17, 34, 35] as a measure of fine scale mixing length. For random points situated on a radius r within the mixing zone, the exit probability data is collected into bins, each holding the data for an interval of possible exit lengths. Using the probability measure $d\xi$, as defined by the binned data, we define $\lambda_C = \int \xi d\xi$. See Fig. 4.2.

We assess interface convergence in terms of the behavior of λ_C. The regime of a resolved momentum equation occurs to the right side of each frame of Fig. 4.2. In this regime, the right frame (with scales independent of Δx) suggests mesh convergence to a limit, with weak dependence on Sc and Pr. In the left frame of Fig. 4.2, we scale out the mesh dependence, and

	l		g		p	
Re	D/D_t	α/α_t	D/D_t	α/α_t	D/D_t	α/α_t
≈ 300	0.031	0.051	39.2	10.4	732	4.16×10^6
≈ 6000	0.002	0.003	1.82	0.307	9.57	1.32×10^4
$\approx 600K$	1.54×10^{-5}	3.41×10^{-5}	0.015	0.002	0.040	27.1

Table 4.1: Ratios of dimensionless molecular to turbulent Schmidt and Prandtl numbers for various cases, all with the finest grid. Ratios large relative to unity indicate resolution of the associated transport equation. The momentum equation has full resolution for $Re \approx 300$ only.

observe that $\lambda_{C\ \mathrm{mesh}}$ is only weakly dependent on Δx in the LES regime (left part of the frame). In other words, $\lambda_C \equiv \lambda_{C\ \mathrm{mesh}} \Delta x$, for an LES simulation, is determined mainly by the mesh level.

We introduce the time dependent molecular diffusion length scales $\lambda_D = 2(D(t-t_0))^{1/2}$, and $\lambda_T = 2(\alpha(t-t_0))^{1/2}$ ($\alpha = \kappa/\rho c_p$), where t_0 is the time of reshock. The corresponding turbulent length scales are $\lambda_{D_t} = 2(D_t(t-t_0))^{1/2}$, and $\lambda_{T_t} = 2(\alpha_t(t-t_0))^{1/2}$. Here $D_t = \nu_{kt}/Sc_t$ and $\alpha_t = \nu_{kt}/Pr_t$ are kinematic turbulent transport coefficients (species and temperature). Sc_t and Pr_t are turbulent transport coefficients and ν_{kt} is the kinematic turbulent viscosity, all defined in Section 2.2. The ratios $(\lambda_D + \lambda_{D_t})/\lambda_C$ and $(\lambda_T + \lambda_{T_t})/\lambda_C$ are dimensionless measures of the concentration and thermal mixing levels due to combined effects of molecular and turbulent transport. We plot these ratios vs. λ_K in Fig. 4.3 for a variety of meshes and for transport coefficients from Table 3.1. The large λ_K asymptote (right side of each frame of Fig. 4.3) represents the limit of a resolved momentum equation. This limit is converged to a grid independent value, which depends on Sc and Pr.

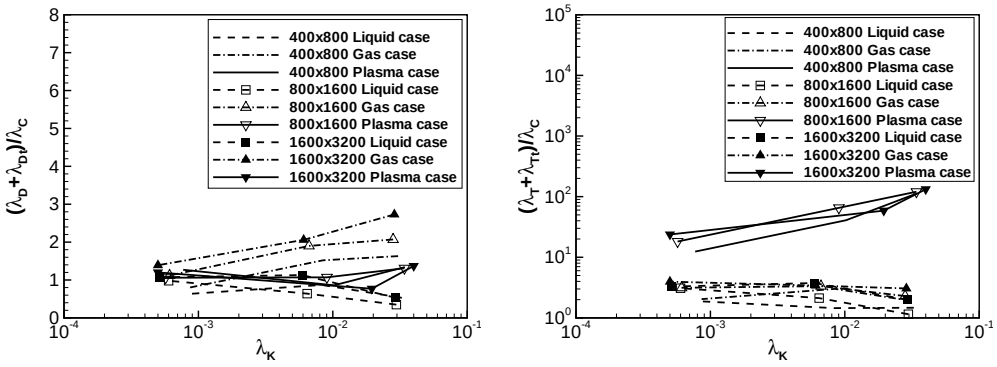

Figure 4.3: The ratios $(\lambda_D + \lambda_{D_t})/\lambda_C$ and $(\lambda_T + \lambda_{T_t})/\lambda_C$ vs. λ_K for several mesh levels and for transport coefficients cases l, g, p from Table 3.1. The values to the far right in each frame are momemtum-resolved, and appear to be mesh converged for the finer meshes.

The ratios are also mesh convergent for higher Re (in the LES regime) and nearly independent of Re. Fig. 4.3 shows the success of the subgrid model, with the mesh converged LES in excellent agreement with momentum-resolved simulations.

It is interesting to compare the ratios of molecular to turbulent length scales. The factor $t - t_0$ cancels and the ratio is just the ratio of the diffusion coefficients, molecular to turbulent. In Table 4.1, we give the ratios of molecular to turbulent transport properties. The ratios are mesh and Reynolds number dependent. Turbulent transport terms are defined in terms of subgrid velocity correlations (with concentration, velocity, or temperature) and are thus logically independent of molecular transport. We tabulate results for the finest mesh only. For the momentum-resolved simulations, the turbulent viscosity terms are neglible, and for high Reynolds number, the turbulent terms

are dominant. Consistent with this picture, we note the virtual identity of the high Reynolds data in Fig. 4.3, at least for the liquid and gas cases.

Chapter 5

Convergence of Micro Observables

5.1 Joint PDFs

The joint pdf for the temperature and species mass concentrations of the fluid mixture is defined as a function of time, assuming that the probability data is collected from the spatial variation of a single realization (single realization of the intial conditions) within the mixing zone. Mixed cells are not averaged, but each cell fraction contributes its own concentration fraction and temperature with its own probabilities (proportional to area). The concentration fractions and temperatures are then binned, with 10 bins per variable.

The liquid and gas joint pdfs are bimodal. Both are concentrated near a curve in concentration-temperature space, joining the light to the heavy fluid concentrations. The origin of this shape can be explained by shock heating, which tends to heat the heavy fluid more strongly, according to the properties of the assumed EOS for the two fluids. This trend is reinforced by the initial conditions; initially the heavy fluid is hotter. Then portions of the

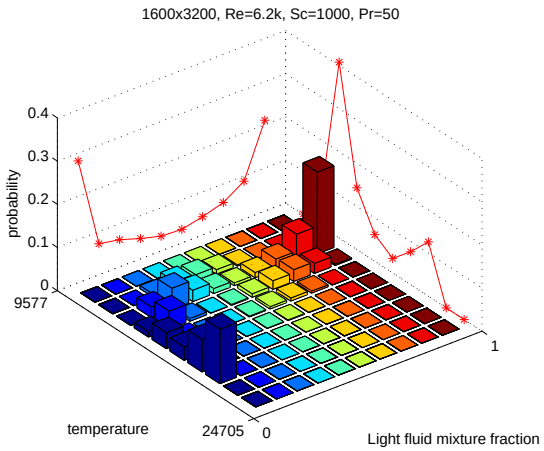

Figure 5.1: Case l. The joint pdf of light species concentration and temperature at time $t = 90$. The data has been collected into 10×10 bins. The mesh is 1600×3200 and $Re \approx 6000$.

heavy and light fluid diffuse into one another, so that the temperature pdf at fixed concentration is determined from the temperature pdf of the pure fluids before mixture through diffusion. The plasma joint pdf is bimodal in its dependence on concentrations, while its temperature dependence is unimodal. See Figs. 5.1, 5.2, 5.3. The data presented is from the time $t = 90$, which is the beginning of the chaotic stage of interface development.

The joint pdfs for temperature-concentration with common physics at three mesh levels are qualitatively similar, and show signs of convergence. See Table 5.1. The mixed region displays some number of large blobs of poorly mixed light material. The relative size of these regions is statistically variable. The errors quoted are measured in the Kolmogorov-Smirnov metric, i.e., the L_∞ norm of the difference of the associated probability distribution functions.

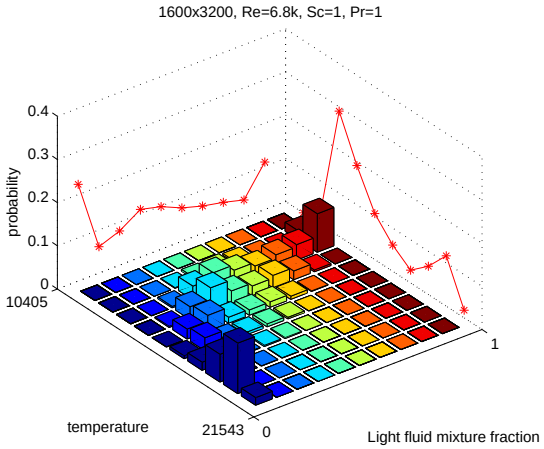

Figure 5.2: Case g. The joint pdf of light species concentration and temperature at time $t = 90$. The data has been collected into 10×10 bins. The mesh is 1600×3200 and $Re \approx 6000$.

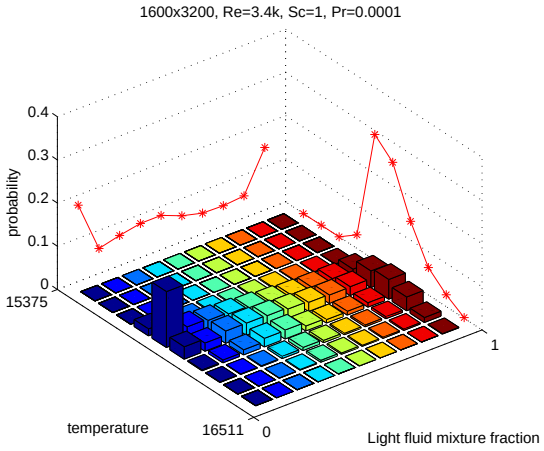

Figure 5.3: Case p. The joint pdf of light species concentration and temperature at time $t = 90$. The data has been collected into 10×10 bins. The mesh is 1600×3200 and $Re \approx 3000$.

	l		g		p	
Re	c to f	m to f	c to f	m to f	c to f	m to f
≈ 300	0.24	0.13	0.08	0.06	0.57	0.31
≈ 6000	0.07	0.06	0.09	0.05	0.68	0.41
$\approx 600K$	0.26	0.06	0.22	0.09	0.14	0.10

Table 5.1: Mesh errors for the joint temperature-concentration pdfs to illustrate possibilities of mesh convergence. Comparison is coarse (c) to fine (f) and medium (m) to fine with pdf's compared using the Kolmogorov-Smirnov metric. Various physical cases reported.

We compute with three distinct meshes (400×800, 800×1600 and 1600×3200) for the cases l, g, and p. Thus there are two levels of error for each case.

The listed Reynolds numbers are approximate, and the refinements are performed (within each series of approximately constant Reynolds number) with identical molecular level transport coefficients. Thus the mesh refinement occurs within identically specified physics. The observed Reynolds numbers and the subgrid scale turbulent transport parameters are mesh dependent, and do vary within this comparison.

5.2 Concentration Moments

Although the errors in the pdfs decrease with mesh refinement, they are not uniformly small, and in the worst cases are as large as the pdfs themselves. For this reason, we next consider a more highly averaged analysis of the same simulation data.

The mean molecular mixing fraction θ, defined [58] as

$$\theta = \frac{\langle f_1 f_2 \rangle}{\langle f_1 \rangle \langle f_2 \rangle} \ , \tag{5.1}$$

is a common measure of mixing. Here f_k is the mass concentration fraction for the species k. Perhaps the best way to understand θ is through its role in the specific chemical reaction production rate w for a simple reaction $A + B \to C$, namely [3]

$$w = \text{const. } f_1 f_2 \exp(-T_{AC}/T) \ , \tag{5.2}$$

where T_{AC} is an activation temperature and w is set to zero if $T < T_{AC}$. The constant in (5.2) is dimensionless. In this formula, we note that θ occurs naturally as a factor in the mean value $\langle w \rangle$ for w. We use moments (θ) to analyze the variability of the concentration, but due to the strongly nonlinear dependence of w on T, we prefer to model T using its pdf. In this way, we analyze the pdf for w with no use of a closure model.

In order to compute the mean value of w, we need to perform the statistical average defining θ at fixed T. This means that we bin together data points with T in a common range (bin), and in this restricted ensemble, we compute means to define θ. Let $\langle \cdot \rangle_T$ denote the expectation in the fixed T spatial ensemble. It is defined as the sum of its argument over all sample points in a fixed T bin divided by the number of sample points in that bin. The result is $\theta(T)$, as a function of temperature T, where

$$\theta(T) = \frac{\langle f_1 f_2 \rangle_T}{\langle f_1 \rangle_T \langle f_2 \rangle_T} \ . \tag{5.3}$$

	l		g		p	
≈ 300	0.09	0.09	0.03	0.01	0.23	0.06
≈ 6000	0.07	0.05	0.14	0.08	0.36	0.15
$\approx 600K$	0.11	0.06	0.12	0.05	0.07	0.07

Table 5.2: Mesh errors for $\theta(T)$, defined by the weighted L_1 norm (5.4). Comparison is coarse (c) to fine (f) and medium (m) to fine. Various physical cases reported.

The result is shown in the nine frames of Fig. 5.4. We note that the gas case has values $\theta(T) \approx 0.6 \ - \ 0.8$ over most of the temperature range. Aside from a peak $\theta(T)$ value associated with the lowest and highest T values (caused by unmixed fluid), most of the $\theta(T)$ range displays very little temperature dependence. Because the θ defined conventionally by a spatial average $\langle \cdot \rangle$ (not constrained to a fixed T value) as in (5.1) is distinct from $\theta(T)$, we include the θ value in each frame of Fig. 5.4. The θ values are generally lower than those obtained in other simulations for related problems. This fact reflects the elimination of numerical mass diffusion in our simulations and a greater occurrence of blobs of unmixed or poorly mixed fluid than is commonly observed numerically.

We supplement the visual convergence shown with a quantitative estimate of the error in $\theta(T)$. See Table 5.2. Here the error is a weighted L_1 norm,

$$e = \int |\theta^c(T) - \theta^f(T)|(dP^c(T) + dP^f(T))/2 \equiv \sum_{i=0}^{9} w_i |\theta_i^c - \theta_i^f| \qquad (5.4)$$

where w_i is the weight of the corresponding temperature bin, calculated (for

	l		g		p	
Re	c to f	m to f	c to f	m to f	c to f	m to f
≈ 300	0.29	0.16	0.06	0.03	0.07	0.01
≈ 6000	0.08	0.07	0.10	0.06	0.20	0.08
$\approx 600K$	0.13	0.03	0.18	0.07	0.03	0.04

Table 5.3: Mesh errors for the specific chemical production w for an activation temperature $T_{AC} = 8,000^oK$. The comparison, based on the Kolmogorov-Smirnov matric, shows mesh convergence. The comparison is coarse mesh (c) to fine (f) and medium (m) to fine. Various physical cases reported.

the coarse to fine comparison) as

$$w_i = \frac{u_i^c + u_i^f}{2}. \tag{5.5}$$

5.3 Temperature PDF

Encouraged by the fact that the variable $\theta(T)$ is mesh convergent, as a factor contributing to the chemistry production term w, we next take the step of analyzing the pdf for T. By definition, this pdf (which we denote $p(T)$), is the number of sample points in a T bin per degree size for the width of the bin in degrees Kelvin. We plot the pdf for T, in Fig. 5.5, for various physical cases.

Again the convergence properties are visually encouraging. Pursuing this point, we tabulate the mesh convergence errors, as measured in the Kolmogorov-Smirnov metric, for the pure T pdf, to show grid convergence, see Table 5.4. The errors for the T pdf are defined as in (5.4).

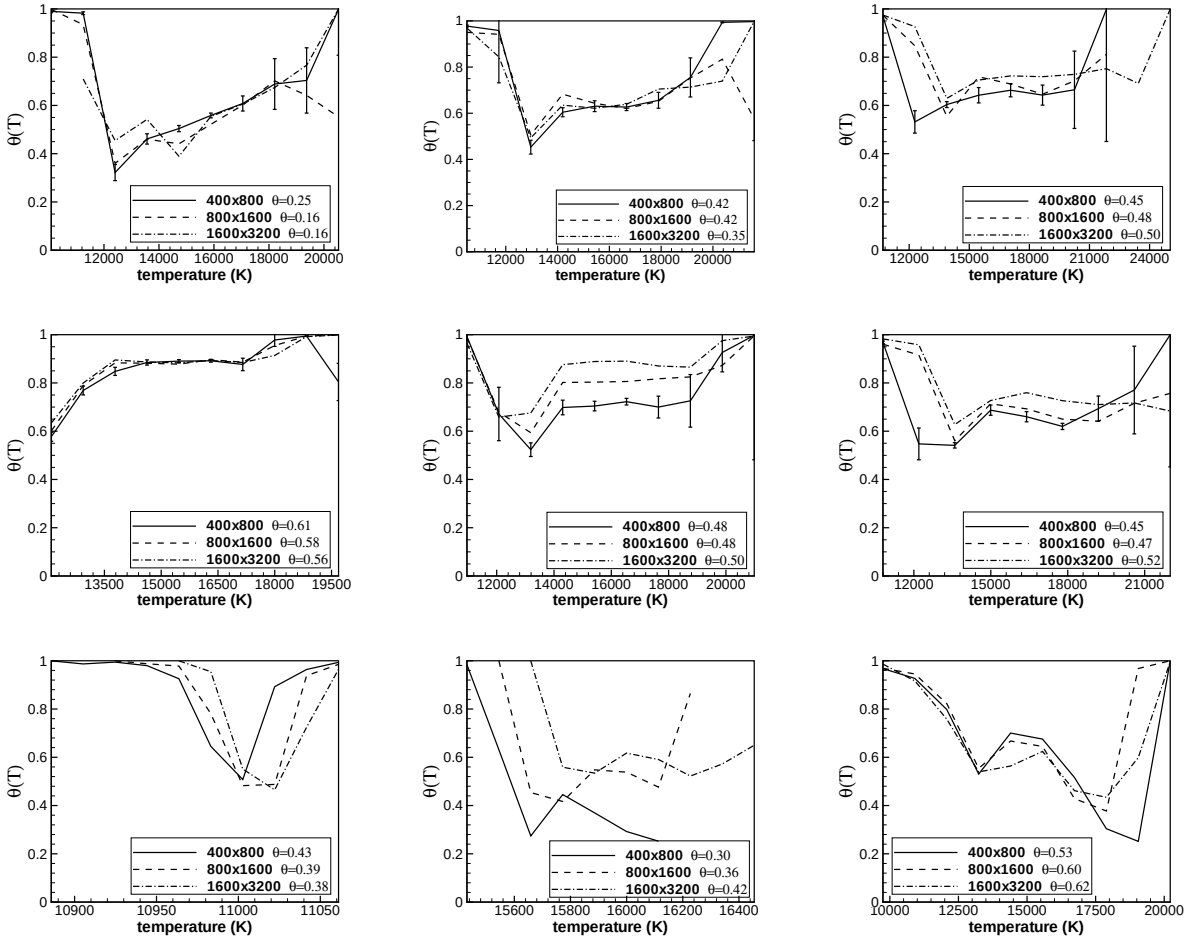

Figure 5.4: Plot of $\theta(T)$ vs. T. Cases l, g, p (rows 1 to 3), with Re increasing, left to right. Error bars indicate coarse grid ensemble fluctuation ($\pm 2\sigma$) centered at the ensemble mean, for cases l, g only.

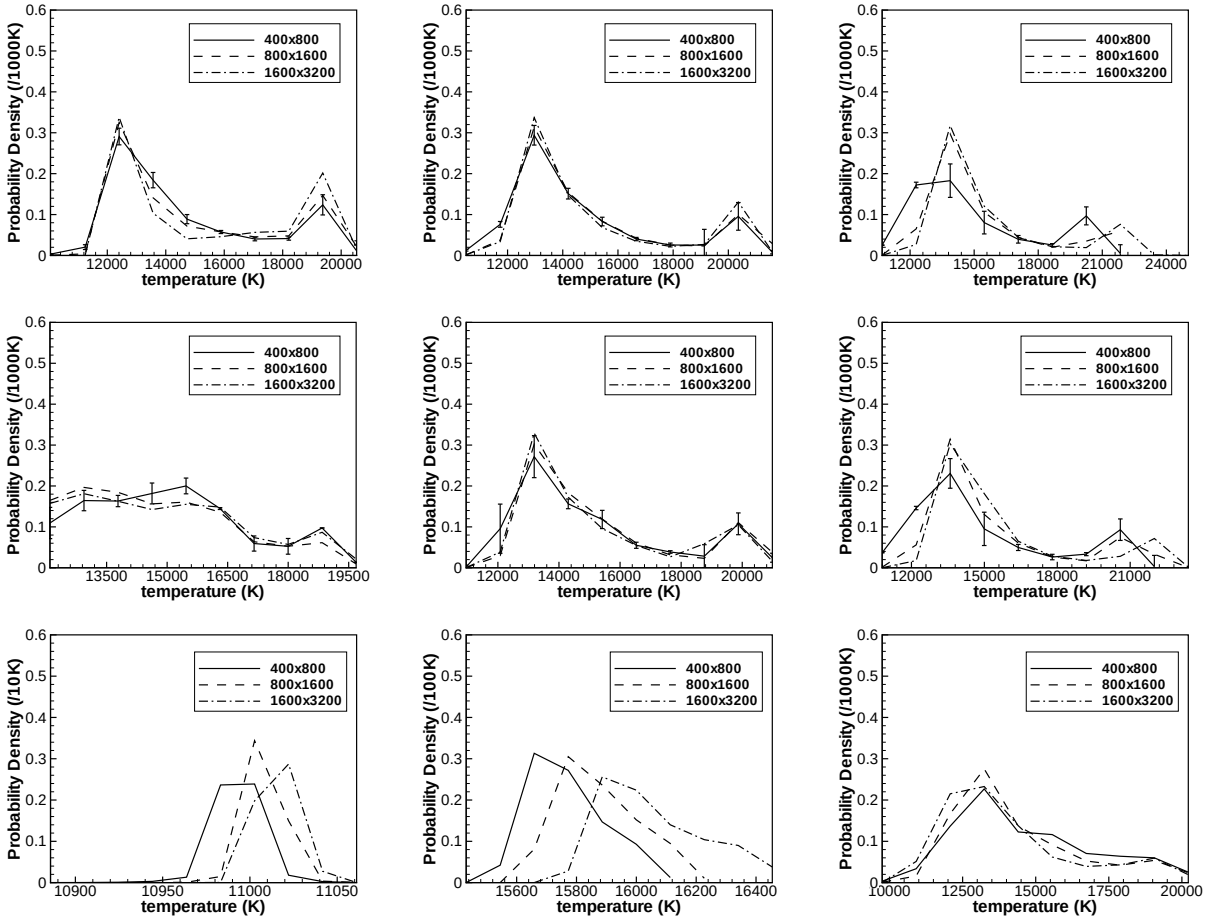

Figure 5.5: Plot of T pdf. Cases l, g, p (rows 1 to 3), with Re increasing, left to right.

	l		g		p	
Re	c to f	m to f	c to f	m to f	c to f	m to f
≈ 300	0.13	0.08	0.05	0.05	0.57	0.31
≈ 6000	0.07	0.03	0.07	0.04	0.68	0.41
$\approx 600K$	0.27	0.06	0.23	0.07	0.13	0.09

Table 5.4: Errors for the temperature pdfs measured in the Kolmogorov-Smirnov metric show mesh convergence. Comparison is coarse mesh (c) to fine (f) and medium (m) to fine. Various physical cases reported.

We note an important distinction between the case p and the cases l and g. For the high thermally diffusive case p, the range of temperatures spatially is very narrow. Accordingly, the convergence of the pdfs in this case is rather like convergence of near delta functions, and as the mesh is varied, there can even be only partial overlap in the temperature ranges observed. The Reynolds number dependence is significant in case p but is weak in cases l and g.

5.4 Chemical Production

Finally, we combine the separate analysis of $\theta(T)$ and T to estimate a convergence rate for the pdf for the specific chemical production w, assuming arbitrarily activation temperatures $T_{AC} = 8,000^o\ K$ and $15,000^o\ K$. Here, $T_{AC} = 8,000^o\ K$ is lower than the range of observed temperatures, while $T_{AC} = 15,000^o K$ is in the middle of the observed temperatures (cases l, g only).

We list convergence properties for the w pdf, based on the Kolmogorov-Smirnov metric in Tables 5.3 and 5.5. The evidence is encouraging, and sug-

	l			g		
Re	$2\sigma/\langle w\rangle$	c to f	m to f	$2\sigma/\langle w\rangle$	c to f	m to f
≈ 300	0.24	0.04	0.03	0.29	0.03	0.02
≈ 6000	0.49	0.04	0.04	0.45	0.03	0.04
$\approx 600K$	0.25	0.09	0.03	0.25	0.09	0.05

Table 5.5: Relative coarse grid ensemble fluctuations ($\pm 2\sigma$) divided by ensemble mean, and mesh errors for the specific chemical production w for an activation temperature $T_{AC} = 15,000^oK$. Comparison based on the Kolmogorov-Smirnov metric. Comparison is coarse mesh (c) to fine (f) and medium (m) to fine. Only cases l and g are reported.

gests convergence, subject to additional mesh refinement. The random variable w displays not only spatical variablity, but also ensemble (realization to realization) variability. Because the temperature range in case p is small, and varies (even to the point of being non-overlapping) as Re and the mesh is varied, it does not seem realistic to choose a T_{AC} within the range of observed temperatures. Accordingly, we omit case p from Table 5.5.

5.5 Statistical Fluctuation vs. Mesh Convergence

Close examination of Tables 5.4 - 5.5 suggests anomalies with the convergence, with a few cases showing only marginal convergence. For this reason we examine the mesh convergence more closely. First, we looked at errors or randomness associated with the binning process. The results did not show significant sensitivity to the binning. Next we examined the radial dependence of the convergence. We found a significant radial dependence on the temperature, a consequence of the fact that the heavy material is hotter than the light.

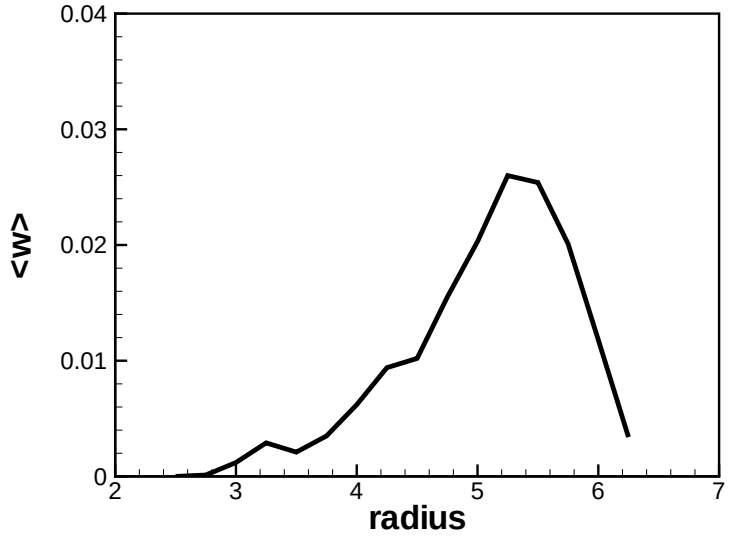

Figure 5.6: Radial dependence for $\langle w \rangle$ for the case l, $Re \approx 6000$.

So the temperature and w, considered as a function of r, is biased towards the outer portion of the mixing zone. See Fig. 5.6. Finally, we considered the relative importance of mesh errors and statistical fluctuations. For the coarsest grid, and for cases l and g only, we introduced a modest ensemble (6 realizations) defined by randomly selected initial perturbations of the interface. We find that the mesh errors are very small, and are dominated by random fluctuations (magnitude defined as 2σ for this small ensemble). Thus we believe that the observed error fluctuations are probably chance events, rather than indicating convergence or its absence. The spatial variabiity of the point values of w, as indicated by its spatial coefficient of variation, typically 100% or more, shows the importance but not the sufficiency of spatial averages.

Chapter 6

Mathematical Existence and Uniqueness Theories

If it is true that numerical solutions to the Euler equations are underdetermined, and that the convergence process produces new structures on each length scale, what is the consequence of these facts for a mathematical existence theory for these equations? It would appear that if such a mathematical solution were to exist, it might not be a function, but a generalized function in the sense of compensated compactness. The compensated compactness generalized functions are pdfs depending on space and time, not dissimilar from what is observed computationally. In the one dimensional existence theory of compensated compactness of DiPerna [45, 46] and Ding and co-workers [4, 8], the first and easier step is to show existence of the generalized solution. The more difficult second step is to show that a generalized solution is a classical (weak) one. In view of the slow rate of progress with the existence theory in two dimensions, and in view of the possibility that this second step might not be correct, it is worth trying to establish generalized compensated compact-

ness solutions without the step of passing to a classical one. Typically such proofs are based on compactness, a method of proof which yields existence but not uniqueness for the weak solutions. We have already commented on the possible nonuniqueness of solutions to the Euler equations. We also note that weak solutions in the form of a space time dependent pdf for the primitive variables are actually what is required scientifically for a combustion simulation. For this reason, such pdf weak solutions couple into the requirements of computational physics, whether they are required as a fundamental scientific truth or not.

Chapter 7

Conclusion

Our most important conclusion is a converging trend for the micro observables for a strongly chaotic mixing flow: reshocked Richtmyer-Meshkov instability. The micro variable mesh convergence is partly obscured by statistical fluctuations, as noted below and in the body of the paper. New computational strategies and new methods of data analysis were required to reach this goal. We have combined (and enhanced) the resolution of sharp gradients near discontinuities of capturing codes with the subgrid physics modeling accuracy of turbulence codes. The convergence properties are basically uniform in Schmidt and Prandtl number. As far as the authors are aware, results of this nature have not been reported by others.

A striking feature of the results is their relative independence on the Reynolds number, allowed to vary by a factor of 2000. Also significant is the strong dependence of the mixing properties of the simulation on the physical regimes with their distinct Schmidt and Prandtl numbers. The impact of diffusion within the simulations is generally lower than commonly reported

on the basis of under resolved untracked capturing codes. Such codes substitute numerical transport properties for physical ones. The actual numerical transport values are not documented, but it is safe to guess that the effective numerical Schmidt and Prandtl numbers are mainly less than one, and thus more diffusive than the present gas case.

These trends in the diffusive properties of the solutions are predicted by the trends in the $(\lambda_D + \lambda_{D_t})/\lambda_C$ and $(\lambda_T + \lambda_{T_t})/\lambda_C$ ratios. In other words, elementary one dimensional diffusion analysis, coupled with a statistical characterization of the flow geometry, is sufficient to predict the major trends observed. We refer to the plot of these ratios in Figs. 4.3.

As new modes of data analysis, we have introduced the importance of convergence for the microscopic variables. These are subject to statistical fluctuations which obscure mesh convergence. Some level of averaging is desirable, but we preserve important nonlinear functionals of the data, for which simple averaging is meaningless. This leads to the ensemble labeled by concentration and temperature values rather than by spatial coordinates. Using this framework and the typical observable of a chemical reaction rate, we observe a reduction of statistical fluctuation and an appearantly converged pdf for the specific chemical reaction rate.

Bibliography

[1] K. Asano. *Mass Transfer: From Fundamentals to Modern Industrial Applications*. Wiley-VCH, 2006.

[2] G. K. Batchelor. Small-scale variation of convected quantities like temperature in turbulent fluid. *J. Fluid Mech*, 5:29–61, 1959.

[3] R. S. Cany and K. Mastorakos. *An Introduction to Turbulent Reacting Flows*. Imperial College Press, London, 2008.

[4] G.-Q. Chen. Convergence of the Lax-Friedrichs scheme for isentropic gas dynamics III. *Acta Mathematica Scienitia*, 6:75–120, 1986.

[5] I-L. Chern and P. Colella. A conservative front tracking method for hyperbolic conservation laws. LLNL Rep. No. UCRL-97200, Lawrence Livermore National Laboratory, 1987.

[6] I-L. Chern, J. Glimm, O. McBryan, B. Plohr, and S. Yaniv. Front tracking for gas dynamics. *J. Comput. Phys.*, 62:83–110, 1986.

[7] P. Colella. A direct Eulerian MUSCL scheme for gas dynamics. *SIAM journal on scientific computing*, 6(1):104–117, 1985.

[8] X. Ding, G.-Q. Chen, and P. Luo. Convergence of the Lax-Friedrichs scheme for isentropic gas dynamics I and II. *Acta Mathematica Scientia*, 5:415–432, 433–472, 1985.

[9] Paul Drake. *Hign energy Density Physics: Fundamentals, Inertial Fusion, and Experimental Astrophysics (Shock Wave and High Pressure Phenomena)*. Springer Verlag, 2006.

[10] Jian Du, Brian Fix, James Glimm, Xicheng Jia, Xiaolin Li, Yunhua Li, and Lingling Wu. A simple package for front tracking. *J. Comput. Phys.*, 213:613–628, 2006. Stony Brook University preprint SUNYSB-AMS-05-02.

[11] S. Dutta, E. George, J. Glimm, J. Grove, H. Jin, T. Lee, X. Li, D. H. Sharp, K. Ye, Y. Yu, Y. Zhang, and M. Zhao. Shock wave interactions in spherical and perturbed spherical geometries. *Nonlinear Analysis*, 63:644–652, 2005. University at Stony Brook preprint number SB-AMS-04-09 and LANL report No. LA-UR-04-2989.

[12] R. P. Fedkiw, T. Aslam, B. Merriman, and S. Osher. A non-oscillatory Eulerian approach to interfaces in multimaterial flows (the ghost fluid method). *J. Comput. Phys.*, 152:457–492, 1999.

[13] Ronald P. Fedkiw and Xu-Dong Liu. The ghost fluid method for viscous flows. In *Progress in Numerical Solutions of Partial Differential Equations, France*. Arachon, 1998.

[14] M. Germano, U. Piomelli, P. Moin, and W. H. Cabot. A dynamic subgrid scale eddy viscosity model. *Phys Fluids A*, 3:1760–1765, 1991.

[15] J. Glimm, M. J. Graham, J. W. Grove, X.-L. Li, T. M. Smith, D. Tan, F. Tangerman, and Q. Zhang. Front tracking in two and three dimensions. *Comput. Math. Appl.*, 35(7):1–11, 1998.

[16] J. Glimm, J. W. Grove, Y. Kang, T. Lee, X. Li, D. H. Sharp, Y. Yu, K. Ye, and M. Zhao. Statistical Riemann problems and a composition law for errors in numerical solutions of shock physics problems. *SISC*, 26:666–697, 2004. University at Stony Brook Preprint Number SB-AMS-03-11, Los Alamos National Laboratory number LA-UR-03-2921.

[17] J. Glimm, J. W. Grove, X. L. Li, W. Oh, and D. H. Sharp. A critical analysis of Rayleigh-Taylor growth rates. *J. Comput. Phys.*, 169:652–677, 2001.

[18] J. Glimm, J. W. Grove, X.-L. Li, K.-M. Shyue, Q. Zhang, and Y. Zeng. Three dimensional front tracking. *SIAM J. Sci. Comp.*, 19:703–727, 1998.

[19] J. Glimm, J. W. Grove, X.-L. Li, and D. C. Tan. Robust computational algorithms for dynamic interface tracking in three dimensions. *SIAM J. Sci. Comp.*, 21:2240–2256, 2000.

[20] J. Glimm, J. W. Grove, X.-L. Li, and N. Zhao. Simple front tracking. In G.-Q. Chen and E. DiBenedetto, editors, *Contemporary Mathematics*, volume 238, pages 133–149. Amer. Math. Soc., Providence, RI, 1999.

[21] J. Glimm, E. Isaacson, D. Marchesin, and O. McBryan. Front tracking for hyperbolic systems. *Adv. Appl. Math.*, 2:91–119, 1981.

[22] J. Glimm, X.-L. Li, and Y.-J. Liu. Conservative front tracking in higher space dimensions. *Transactions of Nanjing University of Aeronautics and Astronautics*, 18:1–15, 2001. Proceedings of International Workshop on Computational Methods for Continuum Physics and Their Applications (IWCCPA), Nanjing, China.

[23] J. Glimm, X.-L. Li, and Y.-J. Liu. Conservative front tracking in one space dimension. *Contemporary Mathematics*, 295:253–264, 2002. Proceedings of the Joint Summer Research Conference on Fluid Flow and Transport in Porous Media: Mathematical and Numerical Treatment. Report SUNYSB-AMS-01-16.

[24] J. Glimm, X.-L. Li, Y.-J. Liu, Z. L. Xu, and N. Zhao. Conservative front tracking with improved accuracy. *SIAMJNA*, 41:1926–1947, 2003.

[25] J. Glimm, X.-L. Li, Y.-J. Liu, and N. Zhao. Conservative front tracking and level set algorithms. *Proc. National Academy of Sci.*, 98:14198–14201, 2001.

[26] J. Glimm, D. Marchesin, and O. McBryan. Subgrid resolution of fluid discontinuities II. *J. Comput. Phys.*, 37:336–354, 1980.

[27] J. Glimm, D. Marchesin, and O. McBryan. A numerical method for two phase flow with an unstable interface. *J. Comput. Phys.*, 39:179–200, 1981.

[28] J. Glimm and O. McBryan. A computational model for interfaces. *Adv. Appl. Math.*, 6:422–435, 1985.

[29] A. Harten and J. Hyman. Self-adjusting grid methods for one-dimensional hyperbolic conservation laws. Rep. No. LA-9105, Los Alamos National Laboratory, Los Alamos, NM, 1981.

[30] D. J. Hill, C. Pantano, and D. L. Pullin. Large-eddy simulation and multiscale modeling of a Richtmyer-Meshkov instability with reshock. *J. Fluid Mech*, 557:29–61, 2006.

[31] R. L. Holmes, B. Fryxell, M. Gittings, J. W. Grove, G. Dimonte, M. Schneider, D. H. Sharp, A. Velikovich, R. P. Weaver, and Q. Zhang. Richtmyer-Meshkov instability growth: Experiment, simulation, and theory. *J. Fluid Mech.*, 389:55–79, 1999. LA-UR-97-2606.

[32] M. M. Koochesfahani and P. E. Dimotakis. Mixing and chemical reactions in a turbulent liquid layer. *J. Fluid Mech.*, 170:83–112, 1986.

[33] H. Lee, H. Jin, Y. Yu, and J. Glimm. On validation of turbulent mixing simulations of Rayleigh-Taylor mixing. *Phys. Fluids*, 20:1–8, 2008. Stony Brook University Preprint SUNYSB-AMS-07-03.

[34] H. Lim, Y. Yu, J. Glimm, X.-L. Li, and D. H. Sharp. Chaos, transport, and mesh convergence for fluid mixing. *Acta Mathematicae Applicatae Sinica*, 24:355–368, 2008. Stony Brook University Preprint SUNYSB-AMS-07-09 Los Alamos National Laboratory preprint number LA-UR-08-0068.

[35] H. Lim, Y. Yu, H. Jin, D. Kim, H. Lee, J. Glimm, X.-L. Li, and D. H. Sharp. Multi scale models for fluid mixing. *Compu. Methods Appl. Mech. Engrg.*, 197:3435–3444, 2008. Stony Brook University Preprint SUNYSB-AMS-07-05.

[36] J.-J. Liu, J. Glimm, and X.-L. Li. A conservative front tracking method. In F. Asakura, H. Aiso, S. Kawashima, Matsumura A, S. Nishibata, and K. Nishihara, editors, *Hyperbolic Problems: Theory, Numerics, and Applications*, pages 57–62. Yokohama Publishers, Osaka, Japan, 2006.

[37] Jinjie Liu, Hyun-Kyun Lim, James Glimm, and Xiaolin Li. A conservative front tracking method in N-dimensions. *J. of Sci. Comp.*, 31:213–236, 2007. Stony Brook University preprint number SUNYSB-AMS-06-04.

[38] X. F. Liu, Y. H. Li, J. Glimm, and X. L. Li. A front tracking algorithm for limited mass diffusion. *J. of Comp. Phys.*, 222:644–653, 2007. Stony Brook University preprint number SUNYSB-AMS-06-01.

[39] W. E. Lorensen and H. E. Cline. Marching cubes: A high resolution 3D surface construction algorithm. *Computer Graphics*, 21(4):163–169, 1987.

[40] T. Ma. *Large eddy simulation of variable density flows*. Ph.d. thesis, University of Maryland, 2006.

[41] T. O. Masser. *Breaking Temperature Equilibrium in Mixed Cell Hydrodynamics*. Ph.d. thesis, State University of New York at Stony Brook, 2007.

[42] P. Moin, K. Squires, W. Cabot, and S. Lee. A dynamic subgrid-scale model for compressible turbulence and scalar transport. *Phys. Fluids*, A3:2746–2757, 1991.

[43] A. S. Monin and A. M. Yaglom. *Statistical Fluid Mechanics: Mechanics of Turbulence*. MIT Press, Cambridge, MA, 1971.

[44] R. Pember, John Bell, Phillip Colella, William Cruchfield, and Michael Welcome. An adaptive cartesian grid method for unsteady compressible flow in irregular regions. *J. Computational Phys.*, 120:278–304, 1995.

[45] R. Di Perna. Convergence of approximate solutions to conservation laws. *Arch. Rational Mech. Anal.*, 82:27–70, 1983.

[46] R. Di Perna. Compensated compactness and general systems of conservation laws. *Trans. Amer. Math. Soc.*, 292:383–420, 1985.

[47] Heintz Pitsch. Large-eddy simulation of turbulent combustion. *Annual Rev. Fluid Mech.*, 38:453–482, 2006.

[48] A. Polyanin. *Hydrodynamics, Mass and Heat Transfer in Chemical Engineering*, volume 14 of *Topics in Chemical Engineering*. CRC Press, 2002.

[49] G. C. Pomraning. *Linear kinetic theory and particle transport in stochastic mixtures*, volume 7 of *Series on Advances in Mathematics for Applied Sciences*. World Scientific, Singapore, 1991.

[50] G. C. Pomraning. Transport theory in discrete stochastic mixtures. *Advances in Nuclear Science and Technology*, 24:47–93, 1996.

[51] R. Richtmyer and K. Morton. *Difference Methods for Initial Value Problems*. Interscience, New York, second edition, 1967.

[52] H. F. Robey. The effect of viscosity and mass diffusion in hydrodynamically unstable plasma flows. *Phys. of Plasmas*, 11:4123–4133, 2004.

[53] D. H. Sharp. An overview of Rayleigh-Taylor instability. *Physica D*, 12:3–18, 1984.

[54] B. Swartz and B. Wendroff. Aztec: A front tracking code based on Godunov's method. *Appl. Num. Math.*, 2:385–397, 1986.

[55] C. Thomas, S. Kumar, G. Orlicz, and K. Prestridge. An experimental investigation of mixing mechanisms in shock-accelerated flow. *J. Fluid Mech.*, 611:131–150, 2008.

[56] Forman Williams. *Combustion Theory*. Addison-Wesley Co., Reading, 1965.

[57] P. Woodward and P. Colella. Numerical simulation of two-dimensional fluid flows with strong shocks. *J. Comput. Phys.*, 54:115, 1984.

[58] D. L. Youngs. Three-dimensional numerical simulation of turbulent mixing by Rayleigh-Taylor instability. *Phys. Fluids A*, 3:1312–1319, 1991.

[59] Y. Yu, M. Zhao, T. Lee, N. Pestieau, W. Bo, J. Glimm, and J. W. Grove. Uncertainty quantification for chaotic computational fluid dynamics. *J. Comput. Phys.*, 217:200–216, 2006. Stony Brook Preprint number SB-AMS-05-16 and LANL preprint number LA-UR-05-6212.